



City Research Online

City, University of London Institutional Repository

Citation: Tsantani, M., Kriegeskorte, N., Storrs, K., Williams, A. L., McGettigan, C. and Garrido, L. ORCID: 0000-0002-1955-6506 (2021). FFA and OFA encode distinct types of face identity information. *The Journal of Neuroscience*, 41(9), pp. 1952-1969. doi: 10.1523/JNEUROSCI.1449-20.2020

This is the accepted version of the paper.

This version of the publication may differ from the final published version.

Permanent repository link: <https://openaccess.city.ac.uk/id/eprint/25458/>

Link to published version: <http://dx.doi.org/10.1523/JNEUROSCI.1449-20.2020>

Copyright: City Research Online aims to make research outputs of City, University of London available to a wider audience. Copyright and Moral Rights remain with the author(s) and/or copyright holders. URLs from City Research Online may be freely distributed and linked to.

Reuse: Copies of full items can be used for personal research or study, educational, or not-for-profit purposes without prior permission or charge. Provided that the authors, title and full bibliographic details are credited, a hyperlink and/or URL is given for the original metadata page and the content is not changed in any way.

City Research Online:

<http://openaccess.city.ac.uk/>

publications@city.ac.uk

1 **FFA and OFA encode distinct types of face identity information**

2 Abbreviated title: Face identity encoding in FFA and OFA

3
4 **Maria Tsantani (maria.tsantani@gmail.com)¹**

5 Division of Psychology, Department of Life Sciences, Brunel University London, Uxbridge UB8 3PH, UK

6
7 **Nikolaus Kriegeskorte (nk2765@columbia.edu)**

8 Zuckerman Mind Brain Behavior Institute, Columbia University, New York, NY 10027, USA

9
10 **Katherine Storrs (katherine.storrs@gmail.com)**

11 Department of Experimental Psychology, Justus Liebig University, 35390 Giessen, Germany

12
13 **Adrian Lloyd Williams (adrian.williams@brunel.ac.uk)**

14 Division of Psychology, Department of Life Sciences, Brunel University London, Uxbridge UB8 3PH, UK

15
16 **Carolyn McGettigan (c.mcgettigan@ucl.ac.uk)**

17 Speech Hearing and Phonetic Sciences, University College London, London WC1N 1PF, UK

18
19 **Lúcia Garrido (lucia.garrido@city.ac.uk)¹**

20 Division of Psychology, Department of Life Sciences, Brunel University London, Uxbridge UB8 3PH, UK

21
22 ¹Corresponding authors

23
24 [Figures: 7](#)

25 [Tables: 2](#)

26
27
28 **Conflict of interest**

29 The authors declare no competing financial interests.

30 **Acknowledgements**

31 This work was supported by a research grant by the Leverhulme Trust (RPG-2014-392) to
32 LG, NK, and CM. We thank Tiana Rakotonombana, Roxanne Zamyadi, Rasanat Nawaz,
33 and Natasha Baxter for help with stimuli preparation and with testing.

34 Current affiliations: Maria Tsantani: Department of Psychological Sciences, Birkbeck,
35 University of London, London WC1E 7HX, UK; Lúcia Garrido: Department of Psychology,
36 City, University of London, London EC1V 0HB, UK

39

Abstract

40 Faces of different people elicit distinct functional MRI (fMRI) patterns in several face-
41 selective regions of the human brain. Here we used representational similarity analysis to
42 investigate what type of identity-distinguishing information is encoded in three face-
43 selective regions: fusiform face area (FFA), occipital face area (OFA), and posterior
44 superior temporal sulcus (pSTS). In a sample of 30 human participants (22 females, 8
45 males), we used fMRI to measure brain activity patterns elicited by naturalistic videos of
46 famous face identities, and compared their representational distances in each region with
47 models of the differences between identities. We built diverse candidate models, ranging
48 from low-level image-computable properties (pixel-wise, GIST, and Gabor-jet
49 dissimilarities), through higher-level image-computable descriptions (OpenFace deep
50 neural network, trained to cluster faces by identity), to complex human-rated properties
51 (perceived similarity, social traits, and gender). We found marked differences in the
52 information represented by the FFA and OFA. Dissimilarities between face-identities in
53 FFA were accounted for by differences in perceived similarity, social traits, gender, and by
54 the OpenFace network. In contrast, representational distances in OFA were mainly driven
55 by differences in low-level image-based properties (pixel-wise and Gabor-jet
56 dissimilarities). Our results suggest that, although FFA and OFA can both discriminate
57 between identities, the FFA representation is further removed from the image, encoding
58 higher-level perceptual and social face information.

59

60 **Keywords: representational similarity analysis; face identity; FFA; OFA**

61

62

63 **Significance statement**

64 Recent studies using functional magnetic resonance imaging (fMRI) have shown that
65 several face-responsive brain regions can distinguish between different face identities. It is
66 however unclear whether these different face-responsive regions distinguish between
67 identities in similar or different ways. We used representational similarity analysis to
68 investigate the computations within three brain regions in response to naturalistically
69 varying videos of face identities. Our results revealed that two regions, the fusiform face
70 area (FFA) and the occipital face area (OFA), encode distinct identity information about
71 faces. Although identity can be decoded from both regions, identity representations in FFA
72 primarily contained information about social traits, gender, and high-level visual features,
73 whereas OFA primarily represented lower-level image features.

74

75

76

77

Introduction

79 The human brain contains several face-selective regions that consistently respond more to
80 faces than other visual stimuli (Kanwisher et al., 1997; Pitcher et al., 2011; Rossion et al.
81 2012; Khuvis et al., 2018; Axelrod et al., 2019). Functional magnetic resonance imaging
82 (fMRI) has revealed that some of these regions represent different face identities with
83 distinct brain patterns. Specifically, studies using fMRI multivariate pattern analysis have
84 shown that face identities can be distinguished based on their elicited response patterns in
85 the fusiform face area (FFA), occipital face area (OFA), posterior superior temporal sulcus
86 (pSTS), and anterior inferior temporal lobe (Nestor et al. 2011; Verosky et al., 2013;
87 Goesaert & Op de Beeck, 2013; Anzellotti et al., 2014; Axelrod & Yovel, 2015; Zhang et
88 al., 2016; Anzellotti & Caramazza, 2017; Guntupalli et al., 2017; Visconti di Oleggio
89 Castello et al., 2017; Tsantani et al., 2019; see also Davidesco et al. (2014), Ghuman et
90 al. (2014), and Khuvis et al. (2018) for results using intracranial electroencephalography,
91 iEEG). But do these regions represent the same information and, if not, what information
92 is explicitly encoded in each of these face-selective regions?

93 Behaviourally, we distinguish between different faces using the surface appearance of
94 the face, the shape of face features, and their spacing or configuration (e.g. Rhodes,
95 1988; Calder et al., 2001; Yovel & Duchaine, 2006; Russell & Sinha, 2007; Russell et al.,
96 2007; Tardif et al., 2019). In particular, Abudarham and Yovel (2016) recently showed that
97 features such as lip thickness, hair colour, eye colour, eye shape, and eyebrow thickness
98 were crucial in distinguishing between individuals (see also Abudarham et al., 2019).
99 Additionally, we perceive a vast amount of socially-relevant information from faces that
100 can be used to distinguish between different individuals, such as gender, age, ethnicity,
101 social traits (Oosterhof & Todorov, 2008; Sutherland et al. 2013), and even relationships
102 and social network position (Parkinson et al., 2014; 2017). Therefore, if the response
103 patterns in a certain brain region distinguish between two individuals, that region could be
104 representing any one—or a combination of —these dimensions.

105 Like several other studies (see above), Goesaert and Op de Beeck (2013)
106 demonstrated that the FFA, OFA, and a face-selective region in the anterior inferior
107 temporal lobe could all decode between different face identities based on fMRI response
108 patterns. Importantly, the authors further tested what type of face information was
109 *encoded* in these different regions. The authors found that all three regions could
110 distinguish between faces using both configural and featural face information, and
111 therefore all regions seemed to represent similar information. Goesaert and Op de Beeck
112 (2013) also showed that representational distances between different faces in face-
113 selective regions did not correlate with low-level pixel-based information. This study
114 however, used one single image for each person's face, making it difficult to disentangle
115 whether representations in a certain brain region are related to identity *per se* or related to
116 the specific images used.

117 To determine whether brain response patterns represent face identity *per se*, it is
118 necessary to show that patterns generalise across different images of the same person's
119 face, in addition to distinguishing that person's face from the faces of other people.
120 Anzellotti et al (2014) showed that classifiers trained to decode face identities in the FFA,
121 OFA, anterior temporal lobe, and pSTS (later analysed in Anzellotti and Caramazza, 2017)
122 could also decode the same faces from novel viewpoints. Guntupalli et al (2017)
123 additionally showed a hierarchical organisation of the functions of face-selective regions,

124 with the OFA decoding viewpoint of face independently of the face identity, the anterior
125 inferior temporal lobe (and a region in the inferior frontal cortex) decoding face identity
126 independently of the viewpoint, and the FFA decoding both viewpoint and identity
127 information (see also Dubois et al., 2015). Extending these findings and using iEEG in
128 epilepsy patients, Ghuman et al (2014) showed invariant decoding in the FFA across
129 different facial expressions. In contrast, Grossman et al (2019) have recently shown that
130 representational distances between different face identities (computed from brain
131 response patterns recorded from implanted electrodes) were very similar across the OFA
132 and the FFA (in the left hemisphere). Crucially, the representational geometries in both
133 regions were associated with differences in image-level descriptions computed from a
134 deep neural network (VGG-Face), which were not generalisable across different
135 viewpoints of the same person's face. These results thus suggest that the OFA and FFA
136 both represent complex configurations of image-based information and not face identity
137 *per se*.

138 Also using iEEG, Davidesco et al. (2014) further showed that representational distances
139 between face images in the FFA (and to a lesser extent in the OFA) were associated with
140 perceived similarity and characteristics of facial features (such as face area and mouth
141 width), but not with low-level features related to pixel-based information (see also Ghuman
142 et al, 2014). Some fMRI studies have shown that even lower-level stimulus-based
143 properties of face images, such as those computed by Gabor filters, explain significant
144 variance in the representational geometries in the FFA (Carlin & Kriegeskorte, 2017) as
145 well as OFA and pSTS (Weibert et al., 2018). On the other hand, other studies have
146 shown that more high-level information, such as biographical information and social
147 context, affects the similarity of response patterns to different faces in the FFA (Verosky et
148 al., 2013; Collins et al., 2016).

149 There is thus mixed evidence regarding whether different face-selective regions rely on
150 similar or distinct information to distinguish between face identities, and what type of
151 information may be encoded in different regions. In the present study, we used
152 representational similarity analysis (RSA) (Kriegeskorte et al., 2008a; 2008b) to
153 investigate what type of identity-distinguishing information is encoded in different face-
154 selective regions. In our previous work (Tsantani et al., 2019), we showed that famous
155 face-identities could be distinguished in the right FFA, OFA, and pSTS based on their
156 elicited fMRI response patterns. Here, for the same set of famous identities and using the
157 same data as in Tsantani et al (2019), we compared the representational distances
158 between identity-elicited fMRI patterns in these regions with diverse candidate models of
159 face properties that could potentially be used to distinguish between identities.

160 Importantly, we used multiple naturalistically varying videos for each identity that varied
161 freely in terms of viewpoint, lighting, head motion, and general appearance. In addition,
162 our representational distances were cross-validated across different videos, in order to
163 deconfound identity from incidental image properties. By using a large, diverse set of
164 candidate models, based on image properties of the stimuli (*image-computable models*)
165 and on human-rated properties (*perceived-property models*), we were able to determine
166 what types of identity-distinguishing information are encoded in different face-selective
167 regions.

168

Materials and Methods

170 This study involved an fMRI component, in which we measured brain representations of
171 faces and voices, and a behavioural component, in which we collected ratings of the same
172 faces and voices on social traits and perceived similarity. The fMRI part corresponds to
173 the same experiment and data described in Tsantani et al. (2019) and the behavioural part
174 is reported here for the first time. In the present study, we analysed the data related to
175 faces only.

176 Participants

177 We recruited thirty-one healthy right-handed adult participants to take part in two fMRI
178 sessions and a behavioural session (all on separate days, resulting in at least six hours of
179 testing per participant). We did not conduct a formal power analysis as there were no
180 previous studies at the time of the study design that had investigated the main effect
181 described in Tsantani et al. (2019). Our sample size was determined based on similar
182 fMRI studies within the field and on available funding. To ensure adequate exposure to our
183 stimulus set of famous people, participants were required to be native English speakers
184 between 18 and 30 years of age, and to have been resident in the UK for at least 10
185 years. We also independently verified that all participants knew the famous people used in
186 the experiment (please see Tsantani et al., 2019). No inclusion or exclusion criteria were
187 applied based on race or ethnicity, and we did not formally record this information. It has
188 been shown that the other-race effect does not apply to familiar faces (McKone et al.,
189 2007; Zhou & Mondloch, 2016). Participants were recruited at Royal Holloway, University
190 of London, and Brunel University London. One participant was excluded due to excessive
191 head movement in the scanner. The final sample consisted of 30 participants (22 females,
192 8 males) with a mean age of 21.2 years (SD=2.37, range=19-27). Participants reported
193 normal or corrected-to-normal vision and normal hearing, provided written informed
194 consent, and were reimbursed for their participation. The study was approved by the
195 Ethics Committee of Brunel University London.

196 Stimuli

197 The same stimuli were used in the fMRI and behavioural testing, and consisted of videos
198 of the faces and sound recordings of 12 famous individuals, including actors, comedians,
199 TV personalities, pop stars and politicians: Alan Carr, Daniel Radcliffe, Emma Watson,
200 Arnold Schwarzenegger, Sharon Osbourne, Graham Norton, Beyonce Knowles, Barbara
201 Windsor, Kylie Minogue, Barack Obama, Jonathan Ross, and Cheryl Cole. These
202 individuals were selected based on pilot studies that showed that participants (aged
203 between 18 and 30 and living in the UK) could recognise them easily from their faces and
204 voices.

205 For each identity, six silent, non-speaking video clips of their moving face were obtained
206 from videos on YouTube (Figure 1). The six clips were obtained from different original
207 videos. In total, we obtained 72 face stimuli. Face videos were selected so that the
208 background did not provide any cues to the identity of the person. The face videos were
209 primarily front-facing and did not feature any speech but were otherwise unconstrained in
210 terms of facial motion. Head movements included nodding, smiling, and rotating the head.
211 Videos were edited so that they were three seconds long, 640 x 360 pixels, and centred
212 on the bridge of the nose, using Final Cut Pro X (Apple, Inc.).

213 For purposes not related to this study, we also presented 72 voice stimuli, which
214 consisted of recordings of the voices of the same 12 famous individuals (6 clips per
215 identity) obtained from videos on YouTube. Speech clips were selected so that the speech
216 content, which was different for every recording, did not reveal the identity of the speaker.
217 Recordings were edited so that they contained three seconds of speech after removing
218 long periods of silence using Audacity® 2.0.5 recording and editing software
219 (RRID:SCR_007198). The recordings were converted to mono with a sampling rate of
220 44100, low-pass filtered at 10KHz, and root-mean-square (RMS) normalised using Praat
221 (version 5.3.80; Boersma and Weenink 2014; www.praat.org).

222 Participants were familiarised with all stimuli via one exposure to each clip immediately
223 before the first scanning session.

224 **MRI data acquisition and preprocessing**

225 Participants completed two MRI sessions: in each session, participants completed a
226 structural scan, three runs of the main experiment, and functional localiser scans (for face
227 and voice areas, but below we only describe the localiser of face-selective regions).
228 Participants were scanned using a 3.0 Tesla Tim Trio MRI scanner (Siemens, Erlangen)
229 with a 32-channel head coil. Scanning took place at the Combined Universities Brain
230 Imaging Centre (CUBIC) at Royal Holloway, University of London. We acquired whole-
231 brain T1-weighted anatomical scans using magnetization-prepared rapid acquisition
232 gradient echo (MPRAGE) [1.0 x 1.0 in-plane resolution; slice thickness, 1.0mm; 176 axial
233 interleaved slices; PAT, Factor 2; PAT mode, GRAPPA (GeneRalized Autocalibrating
234 Partially Parallel Acquisitions); repetition time (TR), 1900ms; echo time (TE), 3.03ms; flip
235 angle, 11°; matrix, 256x256; field of view (FOV), 256mm].

236 For the functional runs, we acquired T2*-weighted functional scans using echo-planar
237 imaging (EPI) [3.0 x 3.0 in-plane resolution; slice thickness, 3.0mm; PAT, Factor 2; PAT
238 mode, GRAPPA; 34 sequential (descending) slices; repetition time (TR), 2000ms; echo
239 time (TE), 30ms; flip angle, 78°; matrix, 64x64; field of view (FOV), 192mm]. Slices were
240 positioned at an oblique angle to cover the entire brain except for the most dorsal part of
241 the parietal cortex. Each run of the main experiment comprised 293 brain volumes, and
242 each run of the face localizer had 227 brain volumes.

243 Functional images were pre-processed used Statistical Parametric Mapping (SPM12;
244 Wellcome Department of Imaging Science, London, UK; RRID:SCR_007037;
245 <http://www.fil.ion.ucl.ac.uk/spm>) operating in Matlab (version R2013b; MathWorks;
246 RRID:SCR_001622). The first three EPI images in each run served as dummy scans to
247 allow for T1-equilibration effects and were discarded prior to pre-processing. Data from
248 each of the two scanning sessions, which took place on different days, were first pre-
249 processed independently with the following steps for each session. Images within each
250 brain volume were slice-time corrected using the middle slice as a reference, and were
251 then realigned to correct for head movements using the first image as a reference. The
252 participants' structural image in native space was coregistered to the realigned mean
253 functional image, and was segmented into grey matter, white matter, and cerebrospinal
254 fluid. Functional images from the main experimental runs were not smoothed, whereas
255 images from the localiser runs were smoothed with a 4-mm Gaussian kernel (full width at
256 half maximum). To align the functional images from the two scanning sessions, the
257 structural image from the first session was used as a template, and the structural image

258 from the second session was coregistered to this template; we then applied the resulting
259 transformation to all the functional images from the second session.

260 **Functional localisers and definition of regions of interest**

261 Face-selective regions were defined using a dynamic face localiser that presented famous
262 and non-famous faces, along with a control condition consisting of objects and scenes.
263 The stimuli were silent, non-speaking videos of moving faces, and silent videos of objects
264 and scenes, presented in an event-related design. Participants completed between one
265 and two runs of the localiser across the two scanning sessions. The localiser presented
266 different stimuli in each of two runs. For full details of the localiser please see Tsantani et
267 al. (2019).

268 Functional regions of interest (ROIs) were defined using the Group-Constrained
269 Subject-Specific method (Fedorenko et al., 2010; Julian et al., 2012), which has the
270 advantage of being reproducible and reducing experimenter bias by providing an objective
271 means of defining ROI boundaries. Briefly, subject-specific ROIs were defined by
272 intersecting subject-specific localiser contrast images with group-level masks for each ROI
273 obtained from an independent dataset. In this study, we obtained group masks of face-
274 selective regions (right fusiform face area (rFFA), the right occipital face area (rOFA), and
275 the right posterior superior temporal sulcus (rpSTS)) from a separate group of participants
276 who completed the same localiser (for details see Tsantani et al., 2019). We focused on
277 face-selective regions from the right hemisphere because they have been shown to be
278 more consistent and larger compared to the left hemisphere (e.g. Rossion et al., 2012).
279 Our masks are publicly available at <https://doi.org/10.17633/rd.brunel.6429200.v1>.

280 Contrast images were defined for each individual participant. Face-selectivity was
281 defined by contrasting activation to faces versus non-face stimuli using *t*-tests. We then
282 intersected these subject-specific contrasts with the group masks, and extracted all
283 significantly activated voxels at $p < .001$ (uncorrected) that fell within the boundaries of
284 each mask. In cases where the resulting ROI included fewer than 30 voxels, the threshold
285 was lowered to $p < .01$ or $p < .05$. ROIs which included fewer than 30 voxels at the lowest
286 threshold were not included, and this occurred for the rFFA in two participants and for the
287 rOFA in one participant. For full details of size and location of all ROIs, please see
288 Tsantani et al. (2019).

289 [\[Please insert Figure 1 about here\]](#)

290 **Experimental Design and Statistical Analysis**

291 **Main experimental fMRI runs**

292 In the main experimental runs, face stimuli were presented intermixed with voice stimuli
293 within each run in an event-related design. The experiment was programmed using the
294 Psychophysics Toolbox (version 3; RRID:SCR_002881; Brainard 1997; Pelli 1997) in
295 Matlab and was displayed through a computer interface inside the scanner. Participants
296 were instructed to fixate on a small square shape that was constantly present in the centre
297 of the screen. From a distance of 85cm, visual stimuli subtended 20.83 x 12.27 degrees of
298 visual angle on the 1024 x 768 pixel screen.

299 The experiment was presented in two scanning sessions, with three runs in each
300 session. Each run featured two unique videos of the face of each of the 12 identities,

301 presented twice. Each run therefore contained 48 face trials (12 identities x 2 videos x 2
302 presentations), intermixed with 48 voice trials (96 experimental trials in total). In other
303 words, across all three runs within a session, each of the 12 face identities appeared in 12
304 trials, featuring six unique videos of their face. Stimuli were presented in a pseudorandom
305 order that prohibited the succeeding repetition of the same stimulus and ensured that each
306 identity could not be preceded or succeeded by another identity more than once within the
307 same modality. Each trial presented a stimulus for 3000 ms and was followed by a 1000
308 ms ITI (Figure 1).

309 To maintain attention to stimulus identity in the scanner, participants performed an
310 anomaly detection task in which they indicated via button press when they were presented
311 with a famous face or voice that did not belong to one of the 12 famous individuals that
312 they had been familiarised with prior to the experiment. Therefore, each run also included
313 12 randomly presented task trials (six faces & six voices). Finally, each run contained 36
314 randomly interspersed null fixation trials, resulting in a total of 144 trials in each run lasting
315 around 10 minutes.

316 The three experimental runs that were completed in the first scanning session were
317 repeated in the second session with the same stimuli, but in a new pseudorandom order.
318 The task stimuli, however, were always novel for each run. The three runs, which had
319 different face videos, were presented in counterbalanced order across participants in both
320 sessions.

321 **Behavioural session**

322 All participants completed a behavioural session in a laboratory, which took place on a
323 separate day and always after the fMRI sessions had been completed. In this session,
324 participants rated the same faces that they had been presented with in the scanner on
325 perceived social traits and on perceived pairwise visual similarity. Participants also rated
326 voices (the order of tasks was counterbalanced across modality), but these results are not
327 presented here. All tasks and stimuli were presented using the Psychophysics Toolbox
328 and Matlab.

329

330 *Social Trait Judgement Tasks*

331 In the social trait judgement tasks, participants were asked to make judgements about
332 the perceived trustworthiness, dominance, attractiveness, and positive-negative valence of
333 the face identities. There were four blocks, one for each judgement, and their order was
334 counterbalanced across participants. Face stimuli were presented in the centre of the
335 screen. In contrast to the fMRI runs, in which stimuli were presented for the full three
336 seconds of their duration, here all stimuli were only presented for the first 1500 ms of their
337 duration, to reduce testing time.

338 All blocks followed the same trial structure (Figure 1). In each trial, a face identity was
339 presented with three videos — these were presented successively with no gap in between
340 them (total of 4500 ms). Participants were then asked to rate how
341 trustworthy/dominant/attractive/negative-positive the face was, and they were asked to
342 base their judgement on all three videos of the face. The rating scale ranged from 1 (very
343 untrustworthy/non-dominant/unattractive/negative) to 7 (very
344 trustworthy/dominant/attractive/positive) and participants responded using the
345 corresponding keys on the keyboard. There was a 1000ms ITI following the response.

346 Each identity was presented in two trials; one trial presented three face videos
347 randomly selected from the six available, and the other trial presented the remaining three
348 videos. This resulted in 24 trials in each block (12 identities x 2 presentations). The videos
349 within each trial were presented in a random order, and the trial order was also
350 randomised. Trustworthiness was defined as 'able to be relied on as honest and truthful'.
351 Dominance was defined as 'having power and influence over other people'. No definition
352 was deemed necessary for valence or attractiveness. Participants were advised that there
353 was no time limit to their responses and that they should follow their first judgment. The
354 duration of each block was approximately 3 minutes.

355 *Pairwise Visual Similarity Task*

356 In the pairwise similarity task, participants rated the perceived visual similarity of pairs
357 of face identities. Each of the 12 identities was paired with the other 11 identities creating
358 66 identity pairs. Each identity was presented by three videos, randomly selected from the
359 six available videos. Each identity pair was presented in two trials, counterbalancing the
360 presentation order of each identity in the pair. There were therefore 132 trials in each task
361 (66 identity pairs x 2 presentations). The presentation order of the pairwise similarity tasks
362 in relation to the social trait judgement tasks was also counterbalanced across
363 participants.

364 Participants were instructed to rate the similarity between the visual appearance of the
365 two face identities in each pair, focusing on the facial features. Participants were asked to
366 rate how similar the two faces looked on a scale from 1 (very dissimilar) to 7 (very similar).
367 Participants were advised that there was no time limit to their responses and that they
368 should follow their first instinct. Participants were told to ignore similarities between people
369 that were related to biographical or semantic information (e.g. if both identities were
370 actors). Furthermore, to encourage participants to base their judgements on perceptual
371 information, participants were advised to consider to what extent two identities could
372 potentially be related to each other, i.e. be part of the same family, based on how they
373 looked.

374 In each trial, participants were first presented with the three videos of the face of one
375 identity (Figure 1). Following a 500ms fixation screen, they were presented with the three
376 videos of the face of the second identity. Videos for each identity were presented
377 successively with no gap in between. Each video was presented for 1500ms and there
378 was a 1000ms ITI following the response. The presentation order of the trials was
379 randomised. The duration of each task was approximately 30 minutes.

380 **Brain Representational dissimilarity matrices (RDMs)**

381 Representational dissimilarity matrices (RDMs) showing the discriminability of the brain
382 response patterns elicited by the 12 face identities (during the fMRI experimental runs)
383 were created for each individual participant and for each ROI.

384 First, to obtain brain responses at each voxel for each of the 12 face identities, mass
385 univariate time-series models were computed for each participant using a high-pass filter
386 cutoff of 128 seconds and autoregressive AR(1) modelling to account for serial correlation.
387 Regressors modelled the BOLD response at stimulus onset and were convolved with a
388 canonical hemodynamic response function (HRF). We defined a model for each run
389 separately, and for every possible pair of runs within a scanning session (by concatenating
390 the two runs), to create data partitions for cross-validation (described below). Each model
391 contained a regressor for the face of each of the 12 identities, which incorporated the

392 different videos of their face (two per run) and the repetitions of those videos. The model
393 also included regressors for each of the 12 voice identities, task trials, and the six motion
394 parameters obtained during the image realignment preprocessing stage (included as
395 regressors of no interest).

396 Second, within each ROI, we extracted the beta estimates at each voxel for each of the
397 12 face identities. This resulted in 12 vectors of beta values per ROI that described the
398 response patterns (across voxels) elicited by the 12 face identities.

399 Third, these vectors of beta estimates were used to compute 12x12 Face RDMs in
400 face-selective ROIs, in which each cell showed the distance between the response
401 patterns of two identities (Figure 2B). RDMs were computed using the linear discriminant
402 contrast (LDC), a cross-validated distance measure (Nili et al. 2014; Walther et al. 2016),
403 which we implemented using in-house Matlab code and the RSA toolbox (Nili et al. 2014).
404 Two RDMs were created for each ROI, one for each scanning session. Each RDM was
405 computed using leave-one-run-out cross-validation across the three runs, which presented
406 different stimuli for each identity. Therefore, RDMs showed the dissimilarities between
407 face *identities*, rather than specific face videos. In each cross-validation fold, concatenated
408 data from two runs formed partition A, and data from the left-out run formed partition B.
409 For each pair of identities (e.g. ID1 and ID2), partition A was used to obtain a linear
410 discriminant, which was then applied to partition B to test the degree to which ID1 and ID2
411 could be discriminated. Under the null hypothesis, LDC values are distributed around zero
412 when two patterns cannot be discriminated. Values higher than zero indicate higher
413 discriminability of the two response patterns (Walther et al. 2016).

414 The discriminability of face identities in each ROI was computed by calculating the
415 mean LDC across all cells of each participant's RDM, and comparing the mean LDC
416 distances against zero (Tsantani et al., 2019).

417 Full details of this analysis are presented in Tsantani et al (2019) and the data to
418 compute brain RDMs are available at <https://doi.org/10.17633/rd.brunel.6429200.v1>. Here,
419 we used the RDMs for three face-selective regions (rFFA, rOFA, and rpSTS). All three of
420 these regions showed significant discriminability of face identities.

421 **RDMs based on image-computable properties**

422 We computed dissimilarities between the 12 face identities based on visual descriptions of
423 their faces obtained using the models described below. We did not use the full videos as
424 input to these models, but instead extracted one still frame from each face video used in
425 the experiment (typically the first frame in which the full face was visible and the image
426 was not blurred). Thus, we obtained six different images of the face of each identity, taken
427 from the six different videos in which the identity was presented, resulting in 72 images in
428 total.

429 *OpenFace Model*

430 The 'OpenFace' model RDM was computed from low-dimensional face representations
431 obtained from OpenFace (Amos et al., 2016; <http://cmusatyalab.github.io/openface/>).
432 Briefly, OpenFace uses a deep neural network that has been pre-trained (using 500,000
433 faces) to learn the best features or measurements that can group two pictures of the same
434 identity together and distinguish them from a picture of a different identity. We used this
435 pre-trained neural network to generate measurements for each of our face pictures and to
436 compare these measurements between each pair of pictures. OpenFace first performs
437

438 face-detection, identifies pre-specified landmarks, and does an affine transformation so
439 that the eyes, nose and mouth appear in approximately the same location. The faces are
440 then passed on to the pre-trained neural network to generate 128 descriptor
441 measurements for each face. To create an RDM, we used the program's calculated
442 distances between the measurements for each pair of faces images. A value of zero
443 indicates that two images are identical, and values between 0 and 1 suggest that two
444 different images likely show the same person's face. Values higher than 1 indicate that the
445 two images show the faces of two different people. We found that OpenFace performed
446 well at grouping different images of the same person's face compared to images of
447 different people's faces in our image set — Extended Data Figure 2-1 includes full 72x72
448 matrices showing distances between all images, [but these full matrices were not used in](#)
449 [any analysis](#)). To obtain a 12x12 RDM for the 12 identities, which would be comparable to
450 the brain RDMs, we computed the mean of all cells that showed images of the same
451 identity pair (Figure 2C). [The 12x12 RDMs were used in all analyses.](#)

452
453

Gabor-Jet Model

454 The Gabor-Jet model RDM was computed from visual descriptors of face images
455 obtained using the Gabor-Jet model (Biederman & Kalocsai, 1997; Margalit et al., 2016;
456 Yue et al., 2012). This model was designed to simulate response properties of cells in
457 area V1, and has been found to correlate with psychophysical measures of facial similarity
458 (Yue et al., 2012). In addition, Carlin and Kriegeskorte (2017) showed that the dissimilarity
459 of response patterns to different faces in the FFA was predicted by image properties
460 based on Gabor filters. First, we used OpenFace 2.0 (Baltrusaitis et al., 2018) to
461 automatically detect the faces in each image, and the pictures were greyscaled. The
462 Matlab script provided in www.geon.usc.edu/GWTgrid_simple.m was then used to create
463 a 100 x 40 Gabor descriptor for each face. After transforming these matrices into vectors,
464 we computed the Euclidean distance between the vectors from each pair of faces
465 (Extended Data Figure 2-1), and then averaged the distances across all pairs of stimuli
466 that showed the same two identities, [resulting in a 12x12 RDM](#) (Figure 2C).

467
468

GIST Model (Faces only and whole Frames)

469 The Gist model RDMs were computed from visual descriptors of pictures obtained
470 using the GIST model (Oliva and Torralba, 2001). The GIST model estimates information
471 about the spatial envelope of scenes and it is related to perceived dimensions of
472 naturalness, openness, roughness, expansion, and ruggedness. Weibert et al. (2018)
473 showed that the similarity between the representations of different faces in the FFA, OFA,
474 and posterior STS was predicted by the similarity of the different pictures computed using
475 the GIST descriptor model. We extracted GIST descriptors both from the full picture
476 (whole Frames) and just from the face (Faces only - we used the same stimuli as in the
477 Gabor-Jet model). We then used the Matlab script provided in
478 <http://people.csail.mit.edu/torralba/code/spatialenvelope> to compute GIST descriptors for
479 each picture, and computed Euclidean distances between each pair of pictures (Extended
480 Data Figure 2-1). We finally averaged the distances across all pairs of stimuli that showed
481 the same two identities, [resulting in 12x12 RDMs](#) (Figure 2C).

482
483

Pixel Model (Faces only and whole Frames)

484 Finally, we computed model RDMs based on pixel dissimilarity between each pair of
485 pictures. Like for the GIST model, we computed this model both for the full picture (whole
486 Frames) and just for the face (Faces only). We extracted pixel greyscale values for each
487 image, computed Pearson correlations between the vectors of each pair of images, and

488 used correlation distance as the output measure ($1 - r$) (Extended Data Figure 2-1). We
489 finally averaged the distances across all pairs of stimuli that showed the same two
490 identities, resulting in 12x12 RDMs (Figure 2C).

491

492 **RDMs based on Perceived properties**

493 *Social Trait Models: Trustworthiness, Dominance, Attractiveness, Valence, Social Traits*
494 *(All)*

495 RDMs for ratings of the 12 face identities on trustworthiness, dominance, attractiveness,
496 and positive-negative valence were computed using Euclidean distances. For each
497 participant and each social trait, the Euclidean distance between the ratings of each pair of
498 identities was calculated (ratings were averaged across the two trials in which the same
499 identity was presented), resulting in a 12x12 RDM per trait. We then averaged the
500 matrices for the same trait across participants (Figure 2C).

501 We also created 'Social Traits (All)' RDMs combining all four social traits, by calculating
502 the Euclidean distance between all trait ratings for each pair of identities, resulting in a
503 12x12 trait RDM per participant. We then computed the mean matrix for all social traits
504 across participants (Figure 2C).

505 To get estimates of the inter-subject reliability of these models, we computed the
506 correlations between each participant's RDM and the average RDMs across all
507 participants (i.e. the RDMs that we used as models), and then averaged the correlations
508 across participants. The reliabilities were $r=.34$ for Trustworthiness, $r=.48$ for Dominance,
509 $r=.67$ for Attractiveness, $r=.31$ for Valence, and $r=.48$ for Social Traits (All). We also
510 computed the average correlations between each participant's RDM and the average
511 RDM of all remaining participants. These reliabilities were $r=.24$ for Trustworthiness, $r=.42$
512 for Dominance, $r=.63$ for Attractiveness, $r=.20$ for Valence, and $r=.42$ for Social Traits (All).

513 *Perceived Similarity Model*

514 The judgements in the Pairwise Visual Similarity Task indicated the degree of visual
515 similarity between all possible pairs of identities. These ratings were averaged across the
516 two trials in which each identity-pair was presented, and were reverse-coded to match the
517 LDC and Euclidean distance measures, where a higher value indicates higher
518 dissimilarity. The resulting values were arranged into a 12x12 face RDM for each
519 participant and were then averaged across participants (Figure 2C).

520

521 Inter-subject reliability, estimated by computing the average correlation between each
522 participant's RDM and the average RDMs across all participants, was $r=.65$. Reliability
523 computed as the average correlation between each participant's RDM and the average
524 RDM of all remaining participants was $r=.61$.

525

526 *Gender Model*

527 Finally, a 12x12 RDM for gender was constructed by assigning a value of 0 to same
528 gender identity pairs, and a value of 1 to different-gender identity pairs (Figure 2C).

529 Correlations between all 13 models are presented in Figure 2D and Extended Data
530 Figure 2-2.

531

[Please insert Figure 2 about here]

532

533 **Individual model analysis: RSA comparing brain RDMs to candidate model RDMs**
534 **using correlation**

535 For each individual participant and each ROI, we compared the brain RDM for faces with
536 each of the candidate model RDMs defined above using Pearson correlation (Figure 3A).
537 We then tested whether the correlations across participants for each ROI were
538 significantly higher than zero, using two-sided one-sample Wilcoxon signed-rank tests (Nili
539 et al., 2014). P-values were corrected for multiple comparisons using FDR correction
540 ($q=.05$) across all 13 comparisons for each ROI. We also compared the correlations
541 across all pairs of models within each ROI, in order to test which model was the best
542 predictor of the variance in brain RDMs in each ROI. For these pairwise comparisons, we
543 used two-sided Wilcoxon signed-rank tests and only significant FDR corrected values (for
544 78 comparisons) are reported.

545 An estimate of the noise ceiling was calculated for each ROI, in order to estimate the
546 maximum correlation that any model could have with the brain RDMs in each ROI given
547 the existing noise in the data. We estimated the noise ceiling using the procedures
548 described by Nili et al. (2014). The lower bound of the noise ceiling was estimated by
549 calculating the Pearson correlation of the brain RDM for each participant with the average
550 brain RDM across all other participants (after z-scoring the brain RDM for each
551 participant). The upper bound of the noise ceiling was estimated by computing the
552 Pearson correlation of the brain RDM for each participant with the average brain RDM
553 across all participants (after z-scoring the brain RDM for each participant).

554 **Weighted model-combination analysis: Weighted representational modelling**

555 We also used weighted representational modelling (Khaligh-Razavi & Kriegeskorte, 2014;
556 Jozwik et al., 2016; 2017) to combine individual models via reweighting and thus
557 investigate if combinations of different model RDMs could explain more variance in
558 representational geometries than any single model. For each combined model, we used
559 linear non-negative least squares regression (lsqnonneg algorithm in Matlab) to estimate a
560 weight for each component of the combined model. We fitted the weights and tested the
561 performance of the reweighted (combined) model on non-overlapping groups of both
562 participants and stimulus conditions within a cross-validation procedure, and used
563 bootstrapping to estimate the distribution of the combined model's performance (Storrs et
564 al., 2020).

565 We used six different combinations of component models: *Image-computable*
566 properties (OpenFace, GIST, GaborJet, and Pixel), *Social Traits* (comprising a weighted
567 combination of the Trustworthiness, Dominance, Attractiveness, and Valence properties),
568 *Perceived* properties (Trustworthiness, Dominance, Attractiveness, Valence, Perceived
569 Similarity, and Gender), *Low-Level* properties (GIST, GaborJet, and Pixel), *High-Level*
570 properties (Trustworthiness, Dominance, Attractiveness, Valence, Perceived Similarity,
571 Gender, and OpenFace), and *All properties*.

572 Within each crossvalidation fold, data from eight participants for four stimulus identity
573 conditions was assigned to serve as test data, and the remainder was used to fit the
574 weights for each component of each of the six combined models. Because the
575 crossvalidation was performed within a participant-resampling bootstrap procedure, the
576 number of participant data RDMs present in each crossvalidation fold was sometimes
577 smaller than eight (when a participant was not present in the bootstrap) or larger than
578 eight (when a participant was sampled multiple times in the bootstrap). All data from the
579 same participant was always assigned *only* to either the training or test split. A reweighting

580 target RDM was constructed by averaging the training-split participants' RDMs for training-
581 split stimulus conditions, and weights were fitted to the components of each combined
582 model to best predict this target RDM. The six resulting combined models, as well as the
583 13 individual models, were then correlated separately with each of the brain RDMs from
584 test participants for test conditions, using Pearson correlation. The noise ceiling was also
585 computed within every cross-validation fold using the same procedure as for the main
586 analysis. In other words, we correlated (Pearson correlation) each test participant's RDM
587 with the average of all other test RDMs excluding their own (for the lower bound of the
588 noise ceiling) and with the average of all test participants' RDMs including their own (for
589 the upper bound of the noise ceiling). This procedure was repeated for 30 participant
590 crossvalidation folds within 30 stimulus-condition crossvalidation folds to provide a
591 stabilised estimate of the noise ceiling and the performance of each model (Storrs, et al.,
592 2020).

593 The cross-validation procedure was repeated for 1,000 bootstrap resamplings of
594 participants for each face-selective ROI. From the resulting bootstrap distribution, we
595 computed the mean estimate of the lower bound of the noise ceiling, as well as the mean
596 of each model's correlation with human data for both individual models and combined
597 models (Figure 3B). Correlations between model and brain RDMs were considered
598 significantly higher than zero if the 95% confidence interval of the bootstrap distribution did
599 not include zero. Bonferroni correction was applied to correct for multiple comparisons.
600 Finally, we compared each pair of models by testing whether the distributions of the
601 differences between each pair of models contained zero. We only report pairwise
602 differences that were significant after Bonferroni correction. Code for this analysis was
603 adapted from here: https://github.com/tinyrobots/reweighted_model_comparison.

604 **Data and code accessibility**

605 Data and code for main analysis are available here:
606 <https://doi.org/10.25383/city.11890509.v1>

607

608

608 **Results**

609 We tested 30 participants in an fMRI experiment, in which they were presented with faces
610 of 12 famous people (same fMRI data as in Tsantani et al., 2019), and in a separate
611 behavioural experiment, in which participants rated the faces of the same people on
612 perceived similarity and social traits (Figure 1). We then computed representational
613 dissimilarity matrices (RDMs) showing the representational distances between the brain
614 response patterns elicited by the face identities in the face-selective right FFA, OFA, and
615 pSTS. The distance measure that we used to compute the RDMs was the linear
616 discriminant contrast (LDC), which is a crossvalidated estimate of the Mahalanobis
617 distance (Walther et al., 2016). The mean LDC across each RDM showed that response
618 patterns to different face identities were discriminable in all three regions (Tsantani et al.,
619 2019). To investigate the informational content of brain representations of the face
620 identities in each face-selective region, we used RSA (Kriegeskorte et al., 2008a; 2008b)
621 to compare the brain RDMs with a diverse set of candidate model RDMs (Figure 2). We
622 used candidate models based on the physical properties of the stimuli (*image-computable*
623 *models*), including low-level stimulus properties (based on Pixel-wise, GIST (Oliva &
624 Torralba, 2001) and Gabor-jet (Biederman & Kalocsai, 1997) dissimilarities) and higher-

625 level image-computable descriptions obtained from a deep neural network trained to
626 cluster faces according to identity (OpenFace; Amos et al., 2016) (see Methods).
627 Additionally, we used candidate models based on perceived higher-level properties
628 (*perceived-property models*), including Gender and participants' ratings of the face
629 identities on Perceived Similarity and Social traits (Trustworthiness, Dominance,
630 Attractiveness, Valence, and Social Traits (All) — which corresponds to all traits
631 combined) in a behavioural experiment.

632 [\[Please insert Figure 3 about here\]](#)

633 **Individual model analysis**

634 In our main analysis, we computed Pearson's correlations between RDMs in the right
635 FFA, OFA, and pSTS, and each candidate model RDM. Correlations were computed for
636 each individual participant, and then correlations across participants for each model were
637 compared against zero using two-sided one-sample Wilcoxon signed-rank tests. For each
638 ROI and each model that showed significant correlations with participants' brain RDMs,
639 we report below the mean correlation across participants, and the Z statistic and p-value
640 obtained from the signed-rank test, corrected for multiple comparisons using FDR
641 correction. Full results are presented in Figure 3A and [Table 1](#), and individual-subject
642 correlations are presented in [Figure 4](#). We also compared the correlations across all pairs
643 of models using two-sided Wilcoxon signed-rank tests.

644 Brain RDMs in the right FFA had the highest mean correlation with the Perceived
645 Similarity model (mean $r = .11$, $Z = 3.69$, $p = .0002$), followed by perceived Social Traits
646 (All) (mean $r = .10$, $Z = 2.71$, $p = .0067$), the image-computable neural network OpenFace
647 (mean $r = .10$, $Z = 3.46$, $p = .0005$), perceived Attractiveness (mean $r = .09$, $Z = 2.69$, $p =$
648 $.0072$), Gender (mean $r = .09$, $Z = 3.30$, $p = .0010$), and Valence (mean $r = .06$, $Z = 2.39$,
649 $p = .0168$) (Figure 3A). We estimated the lower bound of the noise ceiling as the mean
650 correlation between each participant's FFA RDM and the average of all other participants'
651 FFA RDMs (Nili et al., 2014). This estimates the non-noise variance in the data, and is not
652 overfit to the present data. None of the mean correlations reached the lower bound of the
653 noise ceiling for the FFA ($r = .14$) — this suggests that there could be models outside
654 those tested here that would better explain the representational distances in FFA. Pairwise
655 comparisons showed no significant differences between the correlations of any pairs of
656 models (all $p > .0041$; no significant results after FDR correction).

657 In contrast with the FFA, the brain RDMs in the right OFA had the highest mean
658 correlations with low-level image-computable models. The highest mean correlation was
659 observed with the Pixel-Faces model (mean $r = .22$, $Z = 4.36$, $p < .0001$) (Figure 3A),
660 followed by the Gabor-Jet (mean $r = .20$, $Z = 3.97$, $p < .0001$), Pixel-Frames (mean $r = .11$,
661 $Z = 3.02$, $p = .0026$), GIST-Faces (mean $r = .10$, $Z = 2.22$, $p = .0267$), perceived
662 Attractiveness (mean $r = .09$, $Z = 2.84$, $p = .0045$), Gender (mean $r = .07$, $Z = 2.76$, $p =$
663 $.0058$), and the OpenFace model (mean $r = .07$, $Z = 2.95$, $p = .0032$). None of the mean
664 correlations reached the lower bound of the noise ceiling ($r = .34$). Pairwise comparisons
665 between model correlations revealed that the Pixel-Faces model had significantly higher
666 correlations with the OFA RDMs than all other models (all $p < .0058$, FDR corrected),
667 except for the Gabor-Jet model and the GIST-Faces model. The Gabor-Jet model also
668 had significantly higher correlations with the brain RDMs in OFA than all other models (all
669 $p < .0058$, FDR corrected), except the Pixel-Faces and Pixel-Frames models. Perceived
670 Attractiveness had significantly higher correlations with the OFA RDMs than perceived

671 Valence ($p = .0051$), and Social traits (All) was significantly higher than Trustworthiness
672 and Valence (both $p < .0018$).

673 Finally, we investigated which model best explained the variance in representational
674 distances in the right pSTS. We found no significant correlations between any of the
675 candidate models and the brain RDMs in this region (all $p > .0333$; no significant results
676 after FDR correction) (Figure 3A). None of the models reached the lower bound of the
677 noise ceiling ($r = .13$), and there were no significant differences between models (all $p >$
678 $.0140$; no significant results after FDR correction).

679 [\[Please insert Table 1 about here\]](#)

680 [\[Please insert Figure 4 about here\]](#)

681 These results show a clear distinction between the types of models that were
682 associated with the representational geometries of face-identities in the FFA and OFA.
683 Representational distances of face identities in the FFA were most associated with high-
684 level perceived similarity, gender, and social traits, as well as a high-level model of image-
685 computable properties (OpenFace), whereas representations in OFA were most
686 associated with low-level image-computable properties. To test this directly, we compared
687 the correlation profiles between the two regions. We first averaged all correlations per
688 participant (after Fisher's transformation) for the same type of model (all perceived-
689 property models and all image-computable models) for each ROI (FFA and OFA). In the
690 FFA, the mean correlation with perceived-property models was $.08$ ($SD = .095$) and $.03$
691 ($SD = .109$) with image-computable models. In the OFA, the mean correlation with
692 perceived-property models was $.05$ ($SD = .108$) and $.13$ ($SD = .102$) with image-
693 computable models. We then conducted a 2-by-2 repeated measures ANOVA with ROI
694 and type of model as variables. There was no main effect of ROI ($F(1,27)=3.37$, $p=.0773$)
695 or type of model ($F(1,27)=.36$, $p=.5519$), but there was a significant interaction between
696 the two variables ($F(1,27)=23.75$, $p<.0001$). Pairwise comparisons (using two-sided
697 Wilcoxon signed-rank tests) showed that in the FFA, the correlations with perceived-
698 property models were significantly higher than correlations with image-computable models
699 ($Z = 2.25$, $p = .0242$), whereas in the OFA, correlations with perceived-property models
700 were significantly lower than correlations with image-computable models ($Z = -3.17$, $p =$
701 $.0015$). We also divided the models into low-level properties (GIST, Gabor-Jet, and Pixel)
702 and high-level properties (Trustworthiness, Dominance, Attractiveness, Valence,
703 Perceived Similarity, Gender, and OpenFace), and computed means per participant and
704 per ROI for each of these types of models. In the FFA, there was a mean correlation of $.08$
705 ($SD = .090$) with high-level properties, and of $.02$ ($SD = .157$) with low-level properties. In
706 the OFA, there was a mean correlation of $.05$ ($SD = .102$) with high-level properties, and
707 of $.16$ ($SD = .141$) with low-level properties. A 2-by-2 repeated measures ANOVA showed
708 a significant effect of ROI ($F(1,27)=5.44$, $p=.0274$), no significant effect of model
709 ($F(1,27)=.43$, $p=.5201$), and a significant interaction between the two variables
710 ($F(1,27)=21.64$, $p<.0001$). Pairwise comparisons showed that in the FFA, the correlations
711 with high-level models were significantly higher than correlations with low-level models (Z
712 $= 2.21$, $p = .0272$), whereas in the OFA, correlations with high-level models were
713 significantly lower than correlations with low-level models ($Z = -3.25$, $p = .0011$). These
714 results demonstrate the clear distinct patterns of correlations for the FFA and OFA.

715 [\[Please insert Figure 5 about here\]](#)

716 Our image-computable models used a single image from each video clip. We re-computed
717 all models using 72 images per clip, and averaged the features across all images of the
718 same clip. We then computed distances between video clips in the same manner as
719 before, and averaged distances for each pair of identities, resulting in 12x12 RDMs for
720 each model. The results were very similar when using 72 images per clip compared to one
721 image per clip (Figure 5A). We additionally showed that we obtained similar results to
722 those in Figure 3A when using other similarity measures between RDMs (Spearman
723 correlation, Kendall tau-a), demonstrating that these results are not dependent on using
724 Pearson correlation (Figure 6). Finally, we conducted an additional control analysis using
725 brain RDMs in the same ROIs but built from response patterns to voices of the same
726 individuals, instead of brain responses to faces. There were no significant correlations
727 between any of the model RDMs for faces and brain RDMs for voices after correcting for
728 multiple comparisons in the rFFA (all $p > .040$), rOFA (all $p > .103$), or rpSTS (all $p > .063$)
729 (Figure 7). Pairwise comparisons showed no significant differences between the
730 correlations of any pairs of models (all $p > .034$). The estimated lower bounds of noise
731 ceilings for the voices brain RDMs were very low for rFFA ($r = -.038$) and rOFA ($r = -.001$),
732 and higher for rpSTS ($r = .108$). This control analysis demonstrates that the above results
733 for FFA and OFA are specific to visual stimuli (faces). To conclude, we find that the
734 structure of the model correlations is reliable and is systematically different between the
735 FFA and OFA.

736 [Please insert Figure 6 about here]

737 [Please insert Figure 7 about here]

738 **Weighted model-combination analysis**

739 Although our models accounted for a large portion of the explainable variance (based
740 on the noise ceiling) in brain representations in the right FFA and OFA, none of the mean
741 correlations reached the lower bound of the noise ceiling. It could be that each individual
742 model captured only a portion of the information represented in each brain region, in which
743 case we may be able to fully explain the brain representations by combining multiple
744 models. We thus used weighted representational modelling (Khaligh-Razavi &
745 Kriegeskorte, 2014; Jozwik et al., 2016; Jozwik et al., 2017) to combine sets of models
746 into weighted combinations via crossvalidated fitting on the human data, and to investigate
747 if these combined models resulted in better predictions of the brain dissimilarities in each
748 brain region (see Methods). We considered six different combined models: *Image-*
749 *computable* properties (OpenFace, GIST, GaborJet, and Pixel), *Social Traits* (comprising
750 a weighted combination of the Trustworthiness, Dominance, Attractiveness, and Valence
751 properties), *Perceived* properties (Trustworthiness, Dominance, Attractiveness, Valence,
752 Perceived Similarity, and Gender), *Low-Level* properties (GIST, GaborJet, and Pixel),
753 *High-Level* properties (Trustworthiness, Dominance, Attractiveness, Valence, Perceived
754 Similarity, Gender, and OpenFace), and *All properties*.

755 We used linear non-negative least squares regression to estimate a weight for each
756 component of each combined model. We fitted the weights and tested the performance of
757 the reweighted (combined) model on non-overlapping groups of both participants and
758 stimulus conditions within a cross-validation procedure, and used bootstrapping to
759 estimate the distribution of the combined model's performance (Storrs et al., 2020). Figure
760 3B shows the results of this analysis. P-values were corrected for multiple comparisons
761 using Bonferroni correction. For the FFA, the combined models for Perceived properties
762 and High-Level properties had the highest mean correlations with the brain RDMs, and the

763 individual-subject correlations were significantly above zero. For the OFA, the combined
764 model of all Low-Level properties and that of all image-computable properties had the
765 highest mean correlations with the brain RDMs, although the individual-subject
766 correlations were not significantly above zero after correcting for multiple comparisons.
767 Importantly, however, none of the combined models performed better than the best of the
768 individual models (see full results in [Table 2](#)). Instead, the models with best performance
769 in the previous (main) analysis also showed the highest correlations in this analysis.
770 These results suggest that the models that best explained representational distances in
771 each face-selective region share overlapping variance, given that combining them did not
772 improve model performance. Lastly, replicating the findings of the previous analysis using
773 more stringent statistical methods (crossvalidation across stimuli and participants)
774 provides further evidence of a reliable pattern of model correlations in FFA and OFA that
775 reveals a distinction between the type of information encoded in these two regions.

776 [\[Please insert Table 2 about here\]](#)

777 **Individual differences and idiosyncratic representations**

778 It is possible that there were substantial individual differences in face identity
779 representations that limit the magnitude of the correlations between brain and model
780 RDMs in our analyses. Brain and behavioural representations of face identities could be
781 idiosyncratic and thus characteristic of each individual. We considered below three ways
782 in which we could test this hypothesis.

783 First, we considered whether there were substantial individual differences in brain
784 RDMs. To estimate the lower-bound of the noise ceiling, we had computed inter-subject
785 reliabilities of brain RDMs. If, however, there were substantial individual differences in the
786 brain RDMs, we would expect that representational distances in each of the face-selective
787 ROIs could be highly reliable within each participant but not across participants. We thus
788 computed intra-subject reliabilities of brain RDMs by correlating the brain RDMs
789 calculated independently from two separate testing sessions for each participant, and
790 then averaging the correlations across participants. We note that in all other analyses in
791 the present manuscript, the brain RDMs for each participant corresponded to the average
792 of these two sessions. [For all three face-selective ROIs, we observed intra-subject
793 reliabilities \(rFFA: \$r=.063\$; rOFA: \$r=.079\$; rpSTS: \$r=.094\$ \) that were on average lower than
794 the inter-subject reliabilities \(rFFA: \$r=.135\$; rOFA: \$r=.337\$; rpSTS: \$r=.126\$ — please see
795 \[Table 1\]\(#\)\), suggesting that in fact, in this case, the brain RDMs were not more reliable
796 within each individual.](#) It is important to note, however, that there was much less data to
797 compute intra-subject reliabilities than inter-subject reliabilities.

798 Second, idiosyncratic brain representations could also result in higher correlations
799 between each participant's brain RDM and behavioural RDMs based on their own ratings,
800 compared to the average behavioural RDMs that we used in the main analyses. We thus
801 repeated the main analysis using each individual's own RDMs for the rating-based
802 perceived-property models, namely Perceived Similarity, Trustworthiness, Dominance,
803 Attractiveness, Valence, and Social Traits (All). [The results, however, did not reveal
804 higher correlations when using these participant-specific behavioural models \(Figure 5B\).](#)
805 In contrast, correlations with the participants' individual behavioural models were slightly
806 lower than when using average behavioural models.

807 A third possibility is that idiosyncratic representational geometries could result in the
808 variance of each participant's brain RDMs being best explained by a uniquely weighted

809 combination of candidate models (even if no set of weightings would perform well for all
810 participants). However, we did not have sufficient data per participant to test this
811 possibility here.

812

Discussion

813 We aimed to investigate what information is explicitly encoded in the face-selective right
814 FFA, OFA, and pSTS. We extracted fMRI patterns elicited by famous face identities in
815 these regions, and computed face identity RDMs which showed that face identities could
816 be distinguished based on their elicited response patterns in all three regions. Using RSA,
817 we compared the brain RDMs for the FFA, OFA, and pSTS with multiple model RDMs
818 ranging from low-level image-computable properties (pixel-wise, GIST, and Gabor-jet
819 dissimilarities), through higher-level image-computable descriptions (OpenFace deep
820 neural network, trained to cluster faces by identity), to complex human-rated face
821 properties (perceived visual similarity, social traits, and gender). We found that the FFA
822 and rOFA encode face identities in a different manner, suggesting distinct representations
823 in these two regions. The representational geometries of face identities in the FFA were
824 most associated with high-level properties, such as perceived visual similarity, social traits,
825 gender, and high-level image features extracted with a deep neural network (OpenFace;
826 Amos et al., 2016). In contrast, the representational geometries of faces in the right OFA
827 were most associated with low-level image-based properties, such as pixel similarity and
828 features extracted with Gabor filters that simulate functioning of early visual cortex. While
829 previous studies had shown that low-level properties of images extracted with Gabor filters
830 were associated with representational distances of faces in right FFA (Carlin &
831 Kriegeskorte, 2017; Weibert et al, 2018), our results suggest that representations in right
832 FFA use more complex combinations of stimulus-based features and relate to higher-level
833 perceived and social properties (see also Davidesco et al., 2014). These results inform
834 existing neurocognitive models of face processing (Haxby et al., 2000; Duchaine & Yovel,
835 2015) by shedding light on the much-debated computations of face-responsive regions,
836 and providing new evidence to support a hierarchical organisation of these regions from
837 the processing of low-level image-computable properties in the OFA to higher-level visual
838 features and social information in the FFA.

839 Our initial prediction was that by combining and reweighting different candidate models,
840 we would be better able to explain the brain RDMs. However, we did not find evidence for
841 this in any of our face-selective ROIs. These results suggest that, when more than one
842 model was significantly correlated with the brain RDMs for a certain brain region, they
843 tended to explain overlapping variance in the brain RDMs. For example, while Perceived
844 Similarity and OpenFace both explained the representational geometries in right FFA, their
845 combination did not explain more variance than each model individually. However, our
846 pattern of results suggests a clear distinction between the *types* of models that are
847 associated with representations in the FFA and OFA, with higher-level properties
848 explaining more variance in the FFA, and lower-level image-based properties explaining
849 more variance in the OFA.

850 One crucial aspect of our study is that we used naturalistically varying video stimuli and
851 multiple depictions for each identity. Brain RDMs were built by cross-validating the
852 response patterns across runs featuring different videos of the face of each identity, and
853 behavioural models were based on averages of ratings of multiple videos for each identity.
854 Image-based models were built by calculating dissimilarities between image frames taken

855 from multiple videos of the face of each identity, and then computing the mean
856 dissimilarity across different image pairs featuring the same identity pair. Behavioral
857 studies have demonstrated that participants make more mistakes in “telling together” (i.e.
858 grouping multiple images of the same identity, which is different process from “telling
859 apart”, or distinguishing, between different identities) different photos of the same person
860 when those photos were taken with different cameras, on different days, or with different
861 lighting conditions, compared to when photos were taken on the same day and with the
862 same camera (Bruce et al, 1999, Jenkins et al, 2011). Most previous fMRI studies,
863 however, used very visually similar images, or even just a single image, for each identity,
864 making it difficult to determine whether a brain region represents different *face images* or
865 different *face identities*. Here, by having multiple videos for each person we can be more
866 confident that we are capturing representations of specific identities rather than specific
867 stimuli.

868 Related to the previous point, Abudarham and Yovel (2016) have recently shown that
869 humans are more sensitive in perceiving changes in some face features (such as lip-
870 thickness, hair, eye colour, eye shape, and eyebrow thickness) compared to others (such
871 as mouth size, eye distance, face proportion, skin color). Changes in the former type of
872 features (a.k.a. critical features) are perceived as changes in identity and those features
873 tend to be invariant for different images of the same identity. Interestingly, Abudarham et
874 al (2019) showed that the OpenFace algorithm that we used in the present study also
875 seemed to be capturing those same critical features. Given our results in right FFA, it
876 would be interesting to see whether representations in this region can also distinguish
877 between the processing of the critical and non-critical face features as described by
878 Abudarham and colleagues (2016; 2019).

879 Grossman and colleagues (2019) have also recently shown that representations in the
880 FFA relate to image-computable descriptors from a deep neural network. There are two
881 main differences, however, between our results and those of Grossman et al (2019). First,
882 Grossman et al (2019) found similar representational geometries across all face-selective
883 ventral temporal cortex, and no differentiation between OFA and FFA. One possible
884 reason for this difference is that the authors were only able to define OFA and FFA in the
885 left hemisphere, whereas our face-selective regions were defined in the right hemisphere.
886 Face-selective regions are more consistent and larger in the right hemisphere (e.g.
887 Rossion et al, 2012). A second main difference between our results and those of
888 Grossman et al (2019) is that the deep neural network that we used here showed high
889 generalisation across different images of the same person. OpenFace (Amos et al., 2016)
890 was trained specifically to group together images of the same person and distinguish
891 images of different people, and it performed very well in doing this in our set of stimuli (see
892 Extended Data Figure 2-1), where it showed high generalisation across very variable
893 pictures of the same person. This was not the case with the VGG-Face network used by
894 Grossman et al (2019). Future studies should focus on describing and comparing the
895 image-level descriptions of different types of neural networks.

896 Previous studies have demonstrated that face-selective regions are sensitive to the
897 viewpoint from which faces are presented (Grill-Spector et al., 1999; Axelrod and Yovel,
898 2012; Kietzmann et al., 2012; Ramírez et al., 2014; Dubois et al., 2015; Guntupalli et al.,
899 2017). However, there is also evidence that the FFA, OFA, anterior temporal lobe, and
900 pSTS represent face identity across different viewpoints (Anzellotti et al., 2014; Anzellotti
901 and Caramazza, 2017; Guntupalli et al., 2017). In our video stimuli, the faces were mostly

902 front-facing, but were free to vary in terms of changes in viewpoint (e.g. turning the head
903 to the side during the video). Given that our patterns for each identity were estimated
904 across multiple different videos of their face, it is unlikely that viewpoint alone could
905 explain the differences between identities. Therefore, our results suggest that the FFA and
906 OFA encode information that relate to face identity, beyond viewpoint.

907 We note that the lower bounds on the noise ceiling in our analyses were consistently
908 quite low, especially for FFA and pSTS. However, these values are similar to the lower
909 bounds of the noise ceiling in other studies using RSA (e.g. Carlin & Kriegeskorte, 2017;
910 Jozwik et al., 2016; Thornton & Mitchell, 2017; 2018). We considered whether the low
911 correlations could reflect substantial individual differences in face identity brain
912 representations, but our results did not support this possibility. The low noise ceilings in
913 our study likely reflect the fact that the differences between brain-activity patterns
914 associated with faces of different people are small compared to the differences between
915 patterns associated with different visual categories (e.g. faces and places). Moreover, we
916 used identity-based rather than image-based patterns (by crossvalidating across runs
917 presenting different videos for each identity), and this is likely to have introduced additional
918 variability to the pattern estimates. It is also possible that we needed more data per
919 participant, and future studies should consider ways to increase the amount of explainable
920 variance. A related issue is that the perceived-property models had inter-subject
921 reliabilities that varied between .2 and .6 and thus correlations between these models and
922 brain RDMs would be affected by these low reliabilities.

923 None of the models that we considered here explained the representational geometry of
924 responses in the face-selective right pSTS. It is likely that the pSTS as defined in the
925 present study contains overlapping and interspersed groups of voxels that respond to
926 faces only, voices only, or both faces and voices (Beauchamp et al., 2004) that make the
927 overlapping representational geometry difficult to explain. On the other hand, it is possible
928 that the pSTS represents information about people that we did not consider here, such as
929 idiosyncratic facial movements (Yovel & O'Toole, 2016), emotional and mental states
930 (Thornton et al., 2019), biographical knowledge (Verosky et al., 2013; Collins et al., 2016;
931 Thornton et al., 2019), social distance or network position (Parkinson et al., 2014; 2017),
932 or type of social interactions (Walbrin & Koldewyn, 2019). Future studies may need to
933 explore an even richer set of social, perceptual, and stimulus-based models to better
934 characterise responses in the pSTS (and investigate representations beyond face-
935 selective regions).

936 A limitation of our study was the lack of diversity of our face identities in terms of race
937 and ethnicity (ten identities were White Caucasian and two were Black), which limits the
938 generalisability of our results to faces of different ethnicities. It was essential to our study
939 that our set of celebrities were highly familiar to our sample of young British participants,
940 and they were chosen based on their recognisability (of both faces and voices — please
941 see Tsantani et al., 2019). Future work will need to incorporate more diversity in the face
942 stimuli. This is also crucial when considering the image-computable models. In particular,
943 OpenFace has been developed, trained, and evaluated on databases that contain large
944 proportions of Caucasian faces when compared to other ethnicities. Future work using
945 larger samples of identities should evaluate the biases caused by these procedures, and
946 develop models trained on more representative and diverse databases.

947 To conclude, our study highlights the importance of using multiple and diverse
948 representational models to characterise how face identities are represented in different

949 face-selective regions. Although similar levels of identity decodability were observed in
950 both OFA and FFA (Tsantani et al., 2019), the information explicitly encoded in these two
951 regions is in fact distinct, suggesting that the two regions serve quite different
952 computational roles. Future work attempting to define the computations of cortical regions
953 that appear to serve the same function (e.g. discriminating between identities) would
954 benefit from comparing representations in those regions with multiple and diverse
955 candidate models to reveal the type of information that is encoded.

956

957

958

959

960

961

962

963

964

965

966

967

968

969

970

971

972

973

974

975

976

977

978

References

- 980 Abudarham, N., & Yovel, G. (2016). Reverse engineering the face space:
981 Discovering the critical features for face identification. *Journal of Vision*, 16(3),
982 40-40.
- 983 Abudarham, N., Shkiller, L., & Yovel, G. (2019). Critical features for face
984 recognition. *Cognition*, 182, 73-83.
- 985 Amos, B., Ludwiczuk, B., & Satyanarayanan, M. (2016). Openface: A general-
986 purpose face recognition library with mobile applications. *CMU School of*
987 *Computer Science*, 6, 2.
- 988 Anzellotti, S., & Caramazza, A. (2017). Multimodal representations of person
989 identity individuated with fMRI. *Cortex*, 89, 85-97.
- 990 Anzellotti, S., Fairhall, S. L., & Caramazza, A. (2014). Decoding representations of
991 face identity that are tolerant to rotation. *Cerebral Cortex*, 24(8), 1988–1995.
- 992 Axelrod, V., Rozier, C., Malkinson, T. S., Lehongre, K., Adam, C., Lambrecq, V., ...
993 & Naccache, L. (2019). Face-selective neurons in the vicinity of the human
994 fusiform face area. *Neurology*, 92(4), 197-198.
- 995 Axelrod, V., & Yovel, G. (2012). Hierarchical processing of face viewpoint in
996 human visual cortex. *Journal of Neuroscience*, 32(7), 2442-2452.
- 997 Axelrod, V., & Yovel, G. (2015). Successful decoding of famous faces in the
998 fusiform face area. *PLoS ONE*, 10(2), 19–25.
- 999 Baltrusaitis, T., Zadeh, A., Lim, Y. C., & Morency, L. P. (2018, May). Openface
1000 2.0: Facial behavior analysis toolkit. In *2018 13th IEEE International*
1001 *Conference on Automatic Face & Gesture Recognition (FG 2018)* (pp. 59-66).
1002 IEEE.
- 1003 Beauchamp, M. S., Argall, B. D., Bodurka, J., Duyn, J. H., & Martin, A. (2004).
1004 Unraveling multisensory integration: patchy organization within human STS
1005 multisensory cortex. *Nature neuroscience*, 7(11), 1190-1192.
- 1006 Biederman, I., & Kalocsai, P. (1997). Neurocomputational bases of object and face
1007 recognition. *Philosophical Transactions of the Royal Society of London. Series*
1008 *B: Biological Sciences*, 352(1358), 1203-1219.
- 1009 Calder, A. J., Burton, A. M., Miller, P., Young, A. W., & Akamatsu, S. (2001). A
1010 principal component analysis of facial expressions. *Vision research*, 41(9),
1011 1179-1208.
- 1012 Carlin, J. D., & Kriegeskorte, N. (2017). Adjudicating between face-coding models
1013 with individual-face fMRI responses. *PLoS computational biology*, 13(7),
1014 e1005604.
- 1015 Collins, J. A., Koski, J. E., & Olson, I. R. (2016). More than meets the eye: The
1016 merging of perceptual and conceptual knowledge in the anterior temporal face
1017 area. *Frontiers in human neuroscience*, 10, 189.
- 1018 Davidesco, I., Zion-Golumbic, E., Bickel, S., Harel, M., Groppe, D. M., Keller, C. J.,
1019 ... & Schroeder, C. E. (2014). Exemplar selectivity reflects perceptual
1020 similarities in the human fusiform cortex. *Cerebral cortex*, 24(7), 1879-1893.

- 1021 di Oleggio Castello, M. V., Halchenko, Y. O., Guntupalli, J. S., Gors, J. D., &
1022 Gobbini, M. I. (2017). The neural representation of personally familiar and
1023 unfamiliar faces in the distributed system for face perception. *Scientific*
1024 *reports*, 7(1), 1-14.
- 1025 Dubois, J., de Berker, A. O., & Tsao, D. Y. (2015). Single-unit recordings in the
1026 macaque face patch system reveal limitations of fMRI MVPA. *Journal of*
1027 *Neuroscience*, 35(6), 2791-2802.
- 1028 Duchaine, B., & Yovel, G. (2015). A revised neural framework for face processing.
1029 *Annual Review of Vision Science*, 1, 393-416.
- 1030 Fedorenko, E., Hsieh, P. J., Nieto-Castañón, A., Whitfield-Gabrieli, S., &
1031 Kanwisher, N. (2010). New method for fMRI investigations of language:
1032 defining ROIs functionally in individual subjects. *Journal of neurophysiology*,
1033 104(2), 1177-1194.
- 1034 Ghuman, A. S., Brunet, N. M., Li, Y., Konecky, R. O., Pyles, J. A., Walls, S. A., ...
1035 & Richardson, R. M. (2014). Dynamic encoding of face information in the
1036 human fusiform gyrus. *Nature communications*, 5(1), 1-10.
- 1037 Goesaert, E., & de Beeck, H. P. O. (2013). Representations of facial identity
1038 information in the ventral visual stream investigated with multivoxel pattern
1039 analyses. *Journal of Neuroscience*, 33(19), 8549-8558.
- 1040 Grill-Spector, K., Kushnir, T., Edelman, S., Avidan, G., Itzhak, Y., & Malach, R.
1041 (1999). Differential processing of objects under various viewing conditions in
1042 the human lateral occipital complex. *Neuron*, 24(1), 187-203.
- 1043 Grossman, S., Gaziv, G., Yeagle, E. M., Harel, M., Mégevand, P., Groppe, D. M.,
1044 ... & Malach, R. (2019). Convergent evolution of face spaces across human
1045 face-selective neuronal groups and deep convolutional networks. *Nature*
1046 *communications*, 10(1), 1-13.
- 1047 Guntupalli, J. S., Wheeler, K. G., & Gobbini, M. I. (2017). Disentangling the
1048 representation of identity from head view along the human face processing
1049 pathway. *Cerebral Cortex*, 27(1), 46-53.
- 1050 Haxby, J. V., Hoffman, E. A., & Gobbini, M. I. (2000). The distributed human
1051 neural system for face perception. *Trends in cognitive sciences*, 4(6), 223-233.
- 1052 Jenkins, R., White, D., Van Montfort, X., & Burton, A. M. (2011). Variability in
1053 photos of the same face. *Cognition*, 121(3), 313-323.
- 1054 Julian, J. B., Fedorenko, E., Webster, J., & Kanwisher, N. (2012). An algorithmic
1055 method for functionally defining regions of interest in the ventral visual
1056 pathway. *Neuroimage*, 60(4), 2357-2364.
- 1057 Jozwik, K. M., Kriegeskorte, N., & Mur, M. (2016). Visual features as stepping
1058 stones toward semantics: Explaining object similarity in IT and perception with
1059 non-negative least squares. *Neuropsychologia*, 83, 201-226.
- 1060 Jozwik, K. M., Kriegeskorte, N., Storrs, K. R., & Mur, M. (2017). Deep
1061 convolutional neural networks outperform feature-based but not categorical
1062 models in explaining object similarity judgments. *Frontiers in psychology*, 8,
1063 1726.

- 1064 Kanwisher, N., McDermott, J., & Chun, M. M. (1997). The fusiform face area: a
1065 module in human extrastriate cortex specialized for face perception. *The*
1066 *Journal of Neuroscience*, *17*(11), 4302–11.
- 1067 Khaligh-Razavi, S. M., & Kriegeskorte, N. (2014). Deep supervised, but not
1068 unsupervised, models may explain IT cortical representation. *PLoS*
1069 *computational biology*, *10*(11).
- 1070 Khuvis, S., Yeagle, E. M., Norman, Y., Grossman, S., Malach, R., & Mehta, A. D.
1071 (2018). Face-selective units in human ventral temporal cortex reactivate
1072 during free recall. *BioRxiv*, 487686.
- 1073 Kietzmann, T. C., Swisher, J. D., König, P., & Tong, F. (2012). Prevalence of
1074 selectivity for mirror-symmetric views of faces in the ventral and dorsal visual
1075 pathways. *Journal of Neuroscience*, *32*(34), 11763-11772.
- 1076 Kriegeskorte, N., Mur, M., Ruff, D. A., Kiani, R., Bodurka, J., Esteky, H., ... &
1077 Bandettini, P. A. (2008a). Matching categorical object representations in
1078 inferior temporal cortex of man and monkey. *Neuron*, *60*(6), 1126-1141.
- 1079 Kriegeskorte, N., Mur, M., & Bandettini, P. (2008b). Representational similarity
1080 analysis - connecting the branches of systems neuroscience. *Frontiers in*
1081 *Systems Neuroscience*, *2*, 1–28.
- 1082 Margalit, E., Biederman, I., Herald, S. B., Yue, X., & von der Malsburg, C. (2016).
1083 An applet for the Gabor similarity scaling of the differences between complex
1084 stimuli. *Attention, Perception, & Psychophysics*, *78*(8), 2298-2306.
- 1085 McKone, E., Brewer, J. L., MacPherson, S., Rhodes, G., & Hayward, W. G.
1086 (2007). Familiar other-race faces show normal holistic processing and are
1087 robust to perceptual stress. *Perception*, *36*(2), 224-248.
- 1088 Nestor, A., Plaut, D. C., & Behrmann, M. (2011). Unraveling the distributed neural
1089 code of facial identity through spatiotemporal pattern analysis. *Proceedings of*
1090 *the National Academy of Sciences of the United States of America*, *108*(24),
1091 9998–10003.
- 1092 Nili, H., Wingfield, C., Walther, A., Su, L., Marslen-Wilson, W., & Kriegeskorte, N.
1093 (2014). A Toolbox for Representational Similarity Analysis. *PLoS*
1094 *Computational Biology*, *10*(4). <http://doi.org/10.1371/journal.pcbi.1003553>
- 1095 Oliva, A., & Torralba, A. (2001). Modeling the shape of the scene: A holistic
1096 representation of the spatial envelope. *International journal of computer vision*,
1097 *42*(3), 145-175.
- 1098 Oosterhof, N. N., & Todorov, A. (2008). The functional basis of face evaluation.
1099 *Proceedings of the National Academy of Sciences*, *105*(32), 11087-11092.
- 1100 Parkinson, C., Kleinbaum, A. M., & Wheatley, T. (2017). Spontaneous neural
1101 encoding of social network position. *Nature Human Behaviour*, *1*(5), 1-7.
- 1102 Parkinson, C., Liu, S., & Wheatley, T. (2014). A common cortical metric for spatial,
1103 temporal, and social distance. *Journal of Neuroscience*, *34*(5), 1979-1987.
- 1104 Pitcher, D., Dilks, D. D., Saxe, R. R., Triantafyllou, C., & Kanwisher, N. (2011).
1105 Differential selectivity for dynamic versus static information in face-selective
1106 cortical regions. *Neuroimage*, *56*(4), 2356-2363.

- 1107 Ramírez, F. M., Cichy, R. M., Allefeld, C., & Haynes, J. D. (2014). The neural code
1108 for face orientation in the human fusiform face area. *Journal of*
1109 *Neuroscience*, *34*(36), 12155-12167.
- 1110 Rhodes, G. (1988). Looking at faces: First-order and second-order features as
1111 determinants of facial appearance. *Perception*, *17*(1), 43-63.
- 1112 Rossion, B., Hanseeuw, B., & Dricot, L. (2012). Defining face perception areas in
1113 the human brain: a large-scale factorial fMRI face localizer analysis. *Brain and*
1114 *cognition*, *79*(2), 138-157.
- 1115 Russell, R., Biederman, I., Nederhouser, M., & Sinha, P. (2007). The utility of
1116 surface reflectance for the recognition of upright and inverted faces. *Vision*
1117 *research*, *47*(2), 157-165.
- 1118 Russell, R., & Sinha, P. (2007). Real-world face recognition: The importance of
1119 surface reflectance properties. *Perception*, *36*(9), 1368-1374.
- 1120 Storrs, K. Khaligh-Razavi, S. & Kriegeskorte, N. (2020). Noise ceiling on the
1121 crossvalidated performance of reweighted models of representational
1122 dissimilarity: Addendum to Khaligh-Razavi & Kriegeskorte (2014). *bioRxiv*. doi:
1123 <https://doi.org/10.1101/2020.03.23.003046>
- 1124 Sutherland, C. A., Oldmeadow, J. A., Santos, I. M., Towler, J., Burt, D. M., &
1125 Young, A. W. (2013). Social inferences from faces: Ambient images generate
1126 a three-dimensional model. *Cognition*, *127*(1), 105-118.
- 1127 Tardif, J., Morin Duchesne, X., Cohan, S., Royer, J., Blais, C., Fiset, D., ... &
1128 Gosselin, F. (2019). Use of face information varies systematically from
1129 developmental prosopagnosics to super-recognizers. *Psychological Science*,
1130 *30*(2), 300-308.
- 1131 Thornton, M. A., & Mitchell, J. P. (2017). Consistent neural activity patterns
1132 represent personally familiar people. *Journal of cognitive neuroscience*, *29*(9),
1133 1583-1594.
- 1134 Thornton, M. A., & Mitchell, J. P. (2018). Theories of person perception predict
1135 patterns of neural activity during mentalizing. *Cerebral cortex*, *28*(10), 3505-
1136 3520.
- 1137 Thornton, M., Weaverdyck, M., & Tamir, D. (2019). The brain represents people
1138 as the mental states they habitually experience. *Nature Communications*, *10*,
1139 2291.
- 1140 Tsantani, M., Kriegeskorte, N., McGettigan, C., & Garrido, L. (2019). Faces and
1141 voices in the brain: a modality-general person-identity representation in
1142 superior temporal sulcus. *Neuroimage*, *201*, 116004.
- 1143 Verosky, S. C., Todorov, A., & Turk-Browne, N. B. (2013). Representations of
1144 individuals in ventral temporal cortex defined by faces and biographies.
1145 *Neuropsychologia*, *51*(11), 2100–2108.
- 1146 Walbrin, J., & Koldewyn, K. (2019). Dyadic interaction processing in the posterior
1147 temporal cortex. *NeuroImage*, *198*, 296-302.
- 1148 Walther, A., Nili, H., Ejaz, N., Alink, A., Kriegeskorte, N., & Diedrichsen, J. (2016).
1149 Reliability of dissimilarity measures for multi-voxel pattern analysis.

1150 *NeuroImage*, 137(0), 188–200.
1151 <http://doi.org/10.1016/j.neuroimage.2015.12.012>

1152 Weibert, K., Flack, T. R., Young, A. W., & Andrews, T. J. (2018). Patterns of
1153 neural response in face regions are predicted by low-level image properties.
1154 *Cortex*, 103, 199-210.

1155 Yovel, G., & Duchaine, B. (2006). Specialized face perception mechanisms extract
1156 both part and spacing information: Evidence from developmental
1157 prosopagnosia. *Journal of Cognitive Neuroscience*, 18(4), 580-593.

1158 Yovel, G., & O'Toole, A. J. (2016). Recognizing people in motion. *Trends in*
1159 *cognitive sciences*, 20(5), 383-395.

1160 Yue, X., Biederman, I., Mangini, M. C., Malsburg, C. von der, & Amir, O. (2012).
1161 Predicting the psychophysical similarity of faces and non-face complex shapes
1162 by image-based measures. *Vision Research*, 55, 41–46.

1163 Zhang, H., Japee, S., Nolan, R., Chu, C., Liu, N., & Ungerleider, L. (2016). Face-
1164 selective regions differ in their ability to classify facial expressions.
1165 *Neuroimage*, 130, 77-90.

1166 Zhou, X., & Mondloch, C. J. (2016). Recognizing “Bella Swan” and “Hermione
1167 Granger”: No own-race advantage in recognizing photos of famous
1168 faces. *Perception*, 45(12), 1426-1429.

1169
1170
1171
1172
1173
1174
1175
1176
1177
1178
1179
1180
1181
1182
1183
1184
1185
1186
1187
1188
1189
1190
1191
1192
1193
1194
1195
1196

1197 **Tables**

1198 **Table 1: Results of individual model analysis.** The values in this table correspond to the results presented
 1199 in Figure 3A. For each ROI, we show the mean correlations between brain RDMs with each model, standard
 1200 error (SE), Z statistics from two-sided one-sample Wilcoxon signed-rank tests, and whether correlations
 1201 were significantly higher than zero. We also show the estimated lower and upper bounds of the noise ceiling
 1202 for each ROI. Models are ordered by effect size.

	Pearson correlation between RDMs				Noise ceiling
	Mean <i>r</i>	<i>SE</i>	<i>Z</i>	<i>p</i> < .05 (FDR corrected)	[Lower bound Upper bound]
rFFA					[0.135 0.262]
Perceived Similarity	0.109	0.023	3.689	yes	
Social Traits (All)	0.104	0.031	2.710	yes	
Open Face	0.101	0.023	3.461	yes	
Attractiveness	0.090	0.033	2.687	yes	
Gender	0.086	0.021	3.302	yes	
Valence	0.060	0.023	2.391	yes	
Dominance	0.058	0.030	1.640	no	
Gabor-Jet	0.052	0.049	0.956	no	
Trustworthiness	0.040	0.029	1.594	no	
Pixel-Faces	0.035	0.044	0.865	no	
Pixel-Frames	0.005	0.027	0.159	no	
GIST-Faces	-0.006	0.040	0.114	no	
Pixel-Frames	-0.018	0.041	-0.478	no	
rOFA					[0.337 0.408]
Pixel-Faces	0.221	0.031	4.357	yes	
Gabor-Jet	0.204	0.037	3.968	yes	
Pixel-Frames	0.107	0.031	3.016	yes	
GIST-Faces	0.104	0.043	2.216	yes	
Attractiveness	0.092	0.029	2.843	yes	
Social Traits (All)	0.083	0.031	1.979	no	
Gender	0.074	0.021	2.757	yes	
OpenFace	0.067	0.020	2.952	yes	

Dominance	0.055	0.031	1.546	no
Perceived Similarity	0.039	0.026	1.416	no
GIST-Frames	0.025	0.034	0.746	no
Trustworthiness	0.011	0.025	0.400	no
Valence	-0.016	0.031	-0.573	no

rpSTS

[0.126 0.252]

GIST-Frames	0.075	0.047	1.800	no
Dominance	0.052	0.027	1.800	no
OpenFace	0.040	0.020	2.129	no
Social Traits (All)	0.032	0.026	1.018	no
Pixel-Frames	0.022	0.030	0.956	no
Gender	0.020	0.017	0.956	no
Trustworthiness	0.017	0.032	0.524	no
Attractiveness	0.005	0.024	0.134	no
Valence	0.002	0.031	0.051	no
Pixel-Faces	-0.003	0.035	-0.113	no
Perceived Similarity	-0.008	0.026	-0.072	no
Gabor-Jet	-0.045	0.040	-1.100	no
GIST-Faces	-0.048	0.036	-1.368	no

1203
1204
1205
1206
1207
1208
1209
1210
1211
1212
1213

Table 2: Results of weighted representational modelling analysis. The values in this table correspond to the results presented in Figure 3B. Within each ROI, we show the mean correlations between brain RDMs with each model (individual models and combined models), and whether correlations were significantly higher than zero. We also show the estimated lower and upper bounds of the noise ceiling for each ROI, and whether correlations were significantly below the noise ceiling. Models are ordered by effect size and grouped first by image-computable models, then perceived-property models, and then models that combined both types of properties. RW refers to combined and reweighted models.

	Pearson correlation between RDMs			Noise ceiling	
	Mean r	SE	$p < .05$ (Bonferroni corrected)	[Lower bound Upper bound]	$p < .05$ (Bonferroni corrected)
rFFA				[0.089 0.286]	
Open Face	0.105	0.032	yes		no
Gabor-Jet	0.041	0.042	no		no

Pixel-Faces	0.027	0.040	no	no
Pixel-Frames	0.019	0.036	no	no
GIST-Faces	0.007	0.037	no	no
GIST-Frames	-0.010	0.037	no	no
RW Image-Computable	0.063	0.037	no	no
Perceived Similarity	0.118	0.031	yes	no
Social Traits (All)	0.102	0.035	yes	no
Gender	0.094	0.033	yes	no
Attractiveness	0.091	0.035	no	no
Valence	0.059	0.031	no	no
Trustworthiness	0.049	0.033	no	no
Dominance	0.048	0.034	no	no
RW Social Traits	0.074	0.034	no	no
RW Perceived	0.100	0.033	yes	no
RW Low-Level	-0.006	0.035	no	no
RW High-Level	0.096	0.033	yes	no
RW ALL	0.086	0.035	no	no

rOFA

[0.237
0.372]

Pixel-Faces	0.158	0.041	yes	no
Gabor-Jet	0.138	0.047	yes	no
Pixel-Frames	0.108	0.039	no	yes
GIST-Faces	0.087	0.047	no	no
OpenFace	0.066	0.041	no	yes
GIST-Frames	0.050	0.042	no	yes
RW Image Computable	0.089	0.044	no	no
Gender	0.082	0.041	no	no
Attractiveness	0.075	0.039	no	yes
Social Traits (All)	0.067	0.040	no	yes
Perceived Similarity	0.055	0.039	no	yes
Dominance	0.039	0.038	no	yes

Trustworthiness	0.031	0.040	no	yes
Valence	-0.010	0.041	no	yes
RW Social Traits	0.037	0.040	no	yes
RW Perceived	0.033	0.040	no	yes
RW Low-Level	0.103	0.046	no	no
RW High-Level	0.019	0.040	no	yes
RW ALL	0.059	0.041	no	yes

rpSTS

[0.091
0.277]

GIST-Frames	0.051	0.040	no	no
OpenFace	0.034	0.030	no	no
Pixel-Faces	0.009	0.034	no	no
Pixel-Frames	0.006	0.032	no	no
GIST-Faces	-0.031	0.034	no	no
Gabor-Jet	-0.038	0.037	no	no
RW Image- Computable	0.013	0.036	no	no
Dominance	0.054	0.030	no	no
Social Traits (All)	0.035	0.030	no	no
Trustworthiness	0.026	0.033	no	no
Gender	0.023	0.029	no	no
Valence	0.005	0.033	no	no
Attractiveness	0.003	0.029	no	no
Perceived Similarity	-0.003	0.032	no	no
RW Social Traits	0.026	0.033	no	no
RW Perceived	0.031	0.032	no	no
RW Low-Level	0.010	0.038	no	no
RW High-Level	0.033	0.031	no	no
RW ALL	0.025	0.030	no	no

1214

1215

1216

1217

1218

1219

1220 **Figure captions**

1221 **Figure 1. Examples of face trials in the fMRI and behavioural experiments.** All
1222 experiments presented the same videos of moving, non-speaking, faces of 12 famous
1223 people. For each famous person, we presented six naturalistically varying videos of their
1224 face. In an event-related fMRI task, each trial presented a single face video. This task also
1225 contained trials of the same length featuring voice clips (excluded from the present
1226 analysis), stimuli relating to the anomaly detection task, and fixation (null events). In each
1227 trial of the Social Trait Judgements Tasks (separate tasks for Trustworthiness,
1228 Dominance, Attractiveness, and Valence), participants viewed three videos of the face of
1229 the same identity and judged the intensity of the target trait (on a scale from 1 to 7). In
1230 each trial of the Perceived Similarity Task, participants viewed three videos of one identity
1231 followed by three videos of a different identity and rated their visual similarity (from 1 to 7).
1232 Face videos were presented for their full duration of 3000ms in the fMRI experiment,
1233 whereas only the first 1500ms were presented in the behavioural experiments.

1234

1235 **Figure 2. Brain and model representational dissimilarity matrices (RDMs).** **A:**
1236 **Location in MNI space of the three face-selective regions localised in our**
1237 **participants:** OFA (occipital face area), FFA (fusiform face area), and pSTS (posterior
1238 superior temporal sulcus; all regions in the right hemisphere). These probabilistic maps
1239 were created for illustration purposes (in our analyses, we only used subject-specific
1240 regions of interest (ROIs)) and show all voxels that were present in at least 20% of
1241 participants. **B: Example brain representational dissimilarity matrix (RDM) for the**
1242 **right FFA.** For each ROI and each participant, we computed RDMs showing the
1243 dissimilarity of the brain response patterns between all pairs of identities. Each row and
1244 column represent one identity, and response patterns are based on all six presented
1245 videos of that identity. Each cell shows the linear discriminant contrast distance between
1246 the response patterns of two identities (higher values indicate higher dissimilarity),
1247 crossvalidated across runs presenting different videos of the face of each identity. The
1248 matrix is symmetric around a diagonal of zeros. **C: Model RDMs for *image-computable***
1249 ***properties* (blue) and *perceived properties* (pink).** These models are in the same
1250 format as the brain RDMs and show the dissimilarity between two identities on each
1251 property (see Methods). *Image-computable models* include a neural network trained to
1252 distinguish between face identities (OpenFace), a Gabor-Jet model, Pixel Dissimilarity
1253 (both for faces only — Pixel-Faces, and the whole frames — Pixel-Frames), and a GIST
1254 Descriptor model (both for faces — GIST-Faces, and the whole frames — GIST-Frames).
1255 [The RDMs computed per image \(before averaging across identity\) are shown in Extended](#)
1256 [Data Figure 2-1, though those 72x72 RDMs were not used in any analysis.](#) *Perceived-*
1257 *property models* include perceived social traits (Trustworthiness, Dominance,
1258 Attractiveness, Valence, Social Traits (All)), Perceived Similarity, and Gender. Models
1259 based on participant ratings were averaged across participants. All models were built
1260 based on multiple images (image-computable models) or videos (perceived-property
1261 models) of the face of each identity. For visualisation purposes, all model RDMs were
1262 scaled to a range between zero (no dissimilarity) and one (maximum dissimilarity). **D:**
1263 **Correlations (Pearson) between the different model RDMs.** [The different candidate](#)
1264 [models were compared with each other using Pearson correlation.](#) [Extended Data Figure](#)
1265 [2-2 shows this same matrix with added correlation values.](#)

1266

1267 **Figure 3. FFA and OFA show distinct representational profiles of face identity**
1268 **information. A: Similarity (Pearson correlations) between brain RDMs (in FFA, OFA,**
1269 **and pSTS) and each of the individual candidate models.** Bars show mean correlations
1270 across participants and error bars show standard error. Correlations with image-
1271 computable models are in blue and with perceived-property models are in pink. Horizontal
1272 dashed lines show the lower bound of the noise ceiling. An asterisk above a bar and the
1273 name of the model in bold indicate that correlations with that model were significantly
1274 higher than zero. Correlations with individual models are sorted from highest to lowest.
1275 Horizontal lines above bars show significant differences between the correlations of the
1276 first marked column with the subsequent marked columns (FDR corrected for multiple
1277 comparisons). [Full results are Table 1, and single-subject data are shown in Figure 4.](#) **B:**
1278 **Similarity (Pearson correlations) between brain RDMs (in FFA, OFA, and pSTS) and**
1279 **each of the candidate models in the weighted representational modelling analysis.**
1280 Bars show mean correlations and error bars show standard error across 1,000 bootstrap
1281 samples. Horizontal dashed lines show the lower bound of the noise ceiling, averaged
1282 across bootstrap samples. An asterisk above a bar and the name of the model in bold
1283 indicate that correlations with that model were significantly higher than zero. Correlations
1284 with individual models are blocked by type of model (image-computable models followed
1285 by perceived-property models) and sorted from highest to lowest. RW shows the
1286 combined and reweighted models and appears in light blue for models that combine
1287 image-computable properties, in light pink for models that combine perceived properties,
1288 and in grey for models that combine both types of properties. None of the combined
1289 models outperformed individual models. [Full results are reported in Table 2.](#) The results of
1290 both analyses show that in the FFA, the models that explained most of the variance are
1291 related to high-level properties, such as perceived properties of the stimuli and the image-
1292 computable OpenFace model of face recognition. In contrast, brain RDMs in OFA
1293 correlated mainly with low-level image-computable properties such as pixel dissimilarity
1294 and the Gabor-Jet model. No significant correlations were found in pSTS.

1295

1296 **Figure 4. Similarity between brain RDMs (in FFA, OFA, and pSTS) and each of the**
1297 **candidate models, showing individual participant data.** This figure shows the same
1298 data as Figure 3A, but with added individual data. Circles show correlations for individual
1299 participants. Coloured lines show mean (full lines) and median (dotted lines) correlations
1300 across participants. Correlations with models based on perceived-property models are in
1301 pink, and correlations with image-computable models are in blue. Horizontal black dotted
1302 lines mark the zero correlation point. An asterisk above a bar and the name of the model
1303 in bold indicate correlations that were significantly higher than zero. Correlations with
1304 individual models are sorted from highest to lowest based on the mean correlation across
1305 participants to match the format of Figure 3A.

1306

1307 **Figure 5. Control analyses with modified model RDMs. A: Similarity between brain**
1308 **RDMs (in FFA, OFA, and pSTS) and each of the candidate models, using image-**
1309 **computable models derived from 72 images per video.** Our main analysis in Figure 3A
1310 used a single image per video to compute image-computable models. Here, we repeated
1311 all analyses of image-computable models using 72 frames for each video. We extracted

1312 72 image frames for each video, and applied each model to each image. For each model,
1313 after extracting the features of each image of each video, we averaged the values for all
1314 images belonging to the same video. We then computed distances between videos in the
1315 same manner as before, and averaged distances for each pair of identities. We note that
1316 these results were very similar to the ones using just with one image per video, but some
1317 correlations were lower. **B: Similarity between brain RDMs (in FFA, OFA, and pSTS)
1318 and each of the individual candidate models, using behavioural models based on
1319 individual participant ratings.** The analysis was the same as in Figure 3A, but instead of
1320 using average behavioural RDMs, each participant's brain RDM was correlated to their
1321 own behavioural RDMs for Perceived Similarity, Trustworthiness, Dominance,
1322 Attractiveness, Valence, and Social Traits (All). The pattern of results looked very similar
1323 to the ones in Figure 3A, but correlations with perceived-property models were overall
1324 lower when using each participant's own model RDMs.

1325

1326 **Figure 6. Control analyses using other similarity measures between RDMs.**
1327 **Similarity between brain RDMs (in FFA, OFA, and pSTS) and each of the candidate**
1328 **models using Spearman correlation (A) and Kendall tau-a (B).** These analyses were
1329 identical to the analysis using Pearson correlations (Figure 3A), with the exception that
1330 noise ceiling was computed after rank-transforming the RDMs (Nili et al., 2014). The
1331 pattern of results was similar across all three correlation measures.

1332

1333 **Figure 7. Control analysis with modified brain RDMs. Similarity between brain RDMs**
1334 **for voices (in FFA, OFA, and pSTS) and each of the candidate models for faces.** We
1335 computed representational dissimilarity matrices (RDMs) from response patterns to voices
1336 in the rFFA, rOFA, and rpSTS, and compared them with our model RDMs for faces (same
1337 models as in Figure 2). The voice stimuli belonged to the same 12 identities as the face
1338 stimuli and were presented interspersed among the face videos in the same runs (see
1339 Methods section). RDMs for voice identities were computed using the same procedure as
1340 for face identities (see Methods section) and were compared to model RDMs for faces
1341 using Pearson correlation. Correlations with individual models are sorted from highest to
1342 lowest. None of the correlations were significantly greater than zero after correction for
1343 multiple comparisons. Pairwise comparisons showed no significant differences between
1344 the correlations of any pairs of models.

1345

1346 **Figure 2-1. Image-computable model representational dissimilarity matrices (RDMs)**
1347 **per image.** Model RDMs computed from dissimilarities between images for OpenFace,
1348 Gabor-Jet, Pixel-Faces, Pixel-Frames, GIST-Faces, and GIST-Frames. Each row/column
1349 represents a single image, and images are clustered by identity (6 images for each of the
1350 12 identities). Each cell shows the dissimilarity between the two images in the
1351 corresponding rows and columns, with a value of zero indicating that images are identical.
1352 Matrices are symmetric around a diagonal of zeros. From these models, only the
1353 OpenFace model grouped different images of the same identity as more similar compared
1354 to images from different identities. **Please note that these full RDMs were not used in any**
1355 **analysis. Instead, we created 12x12 RDMs (one entry for each of the 12 identities) to be**

1356 comparable to the brain RDMs (Figure 2C). To create the 12x12 RDMs, we computed the
1357 mean of all cells that showed images of the same identity pair.

1358

1359 **Figure 2-2. Correlations (Pearson) between the different model RDMs.** The different
1360 candidate models were compared with each other using Pearson correlation. This is the
1361 same figure as 2D, but with added correlation values for each cell.

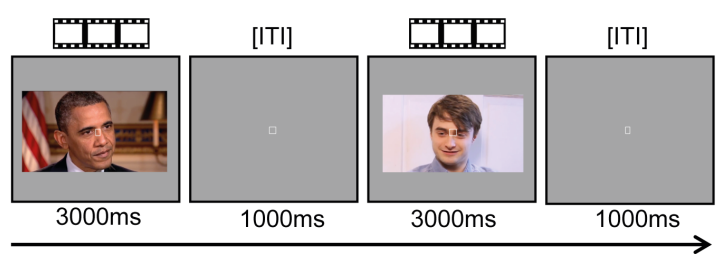
1362

1363

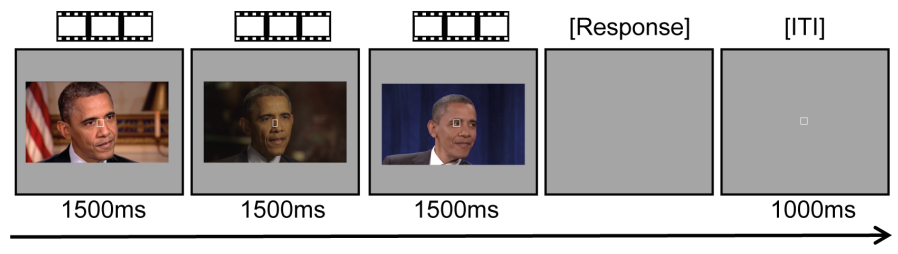
1364

1365

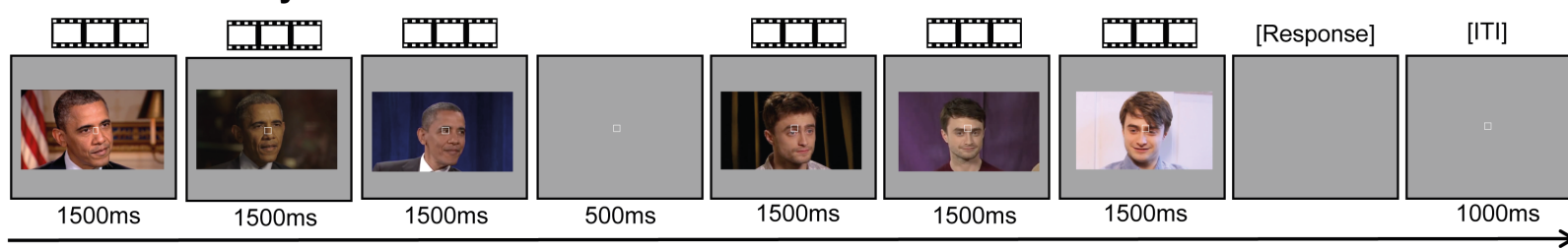
fMRI

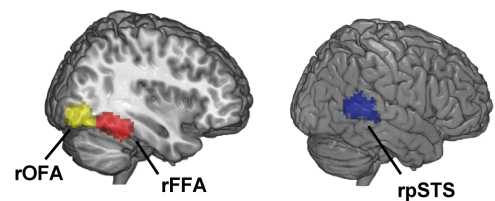
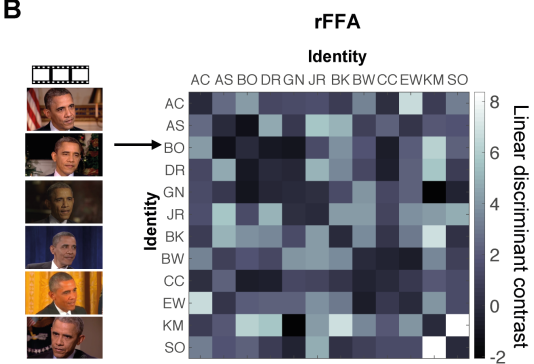
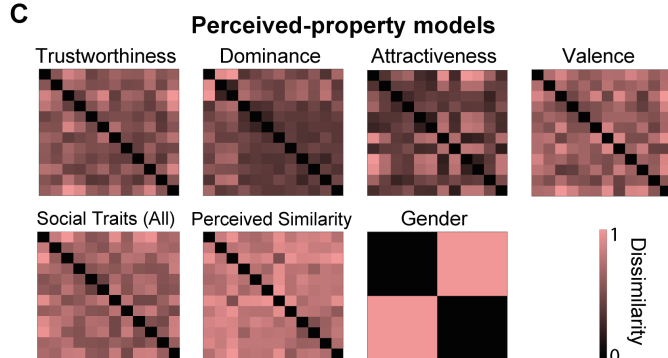
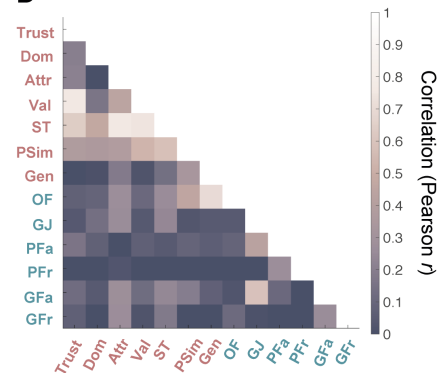


Social Trait Judgements

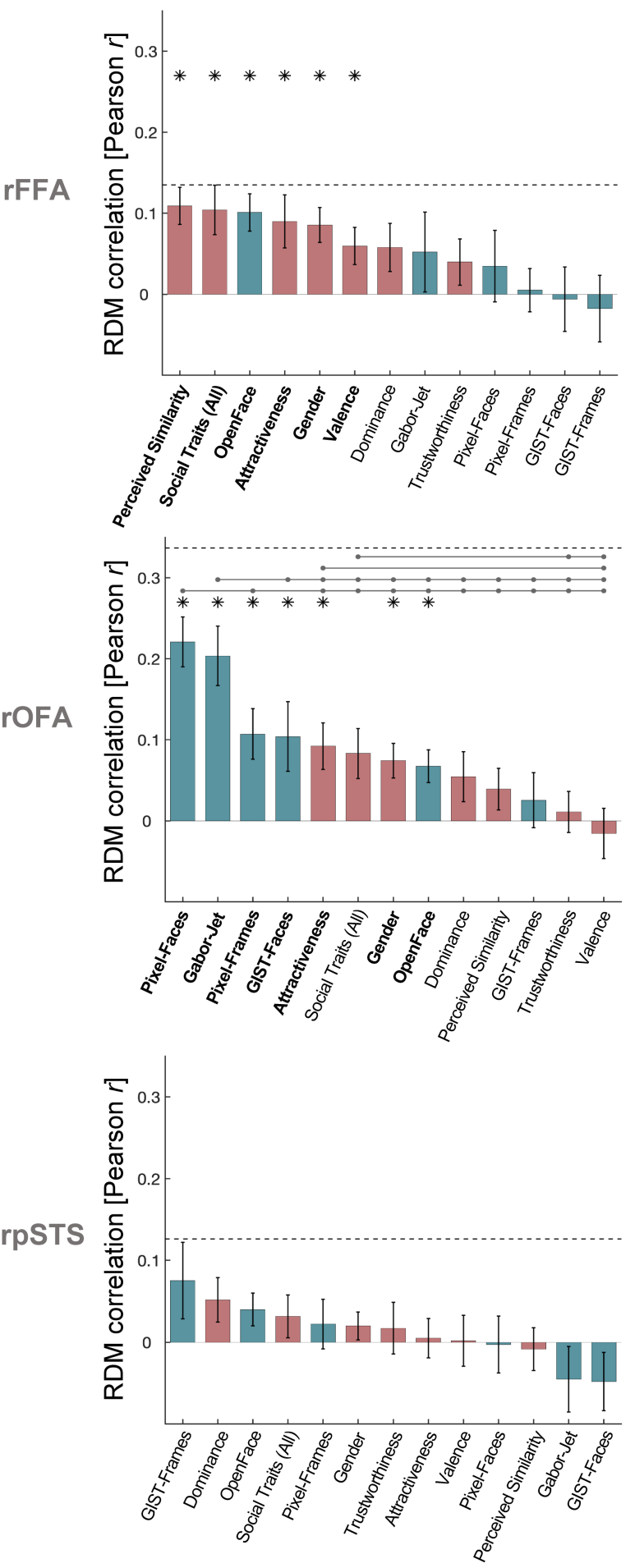


Perceived Similarity

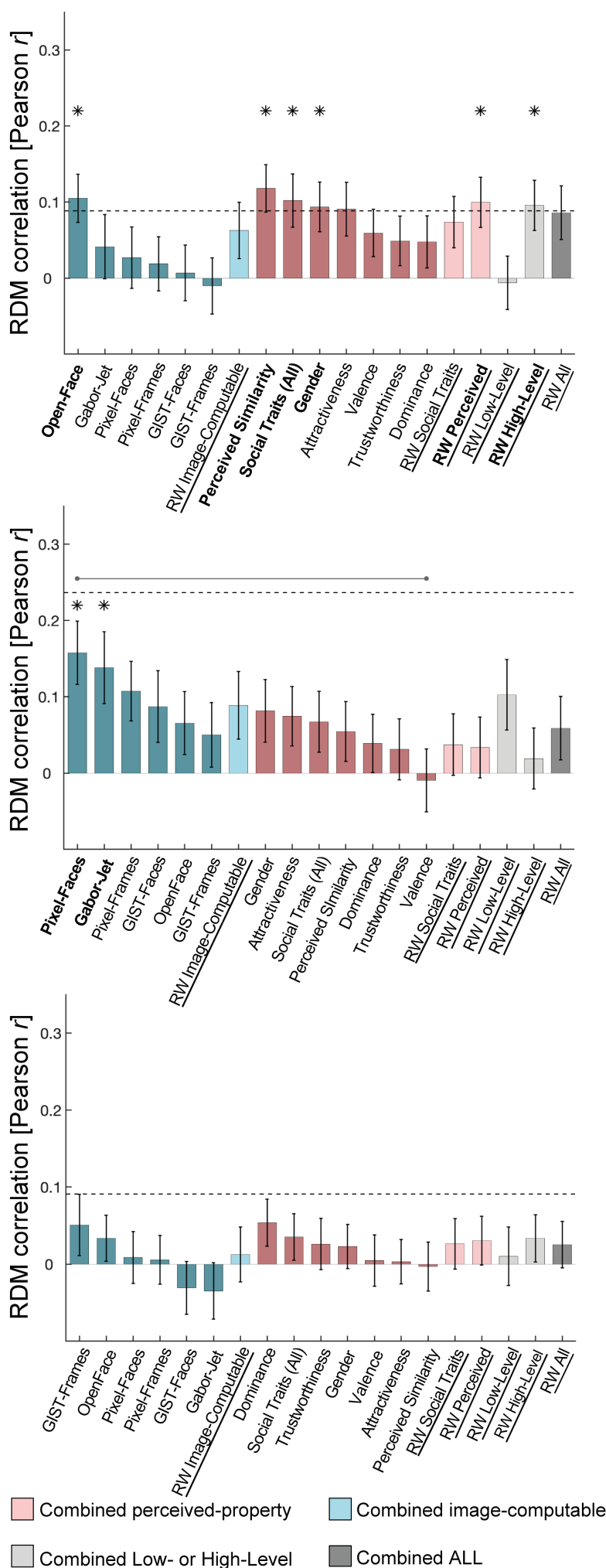


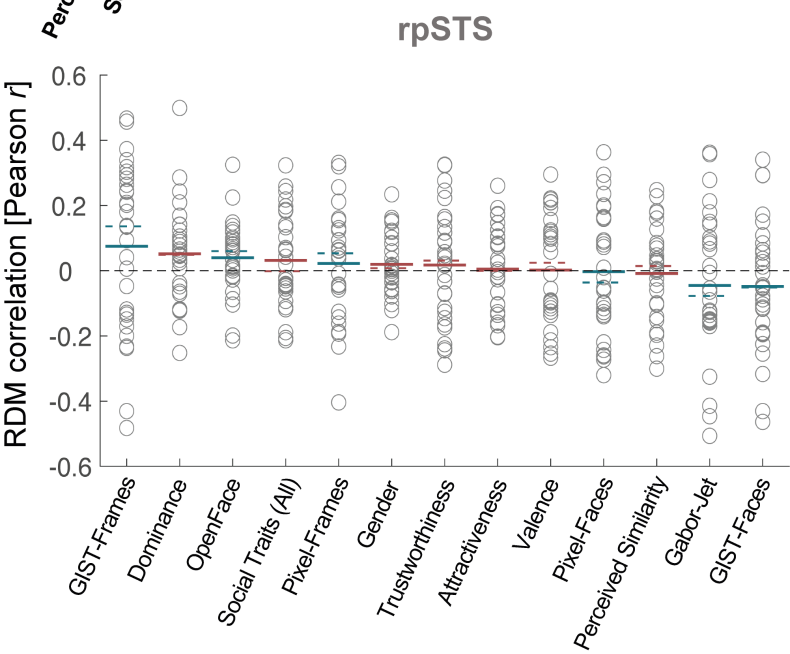
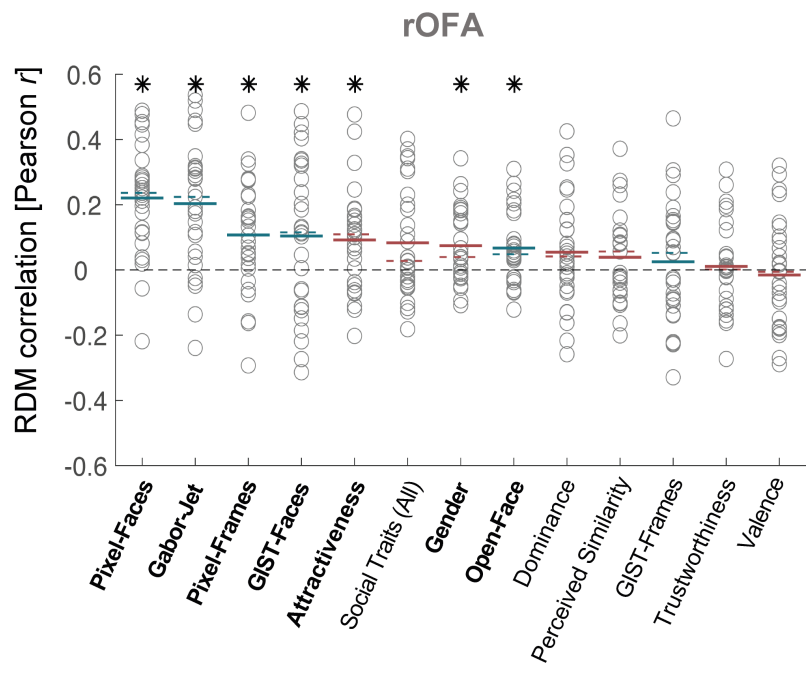
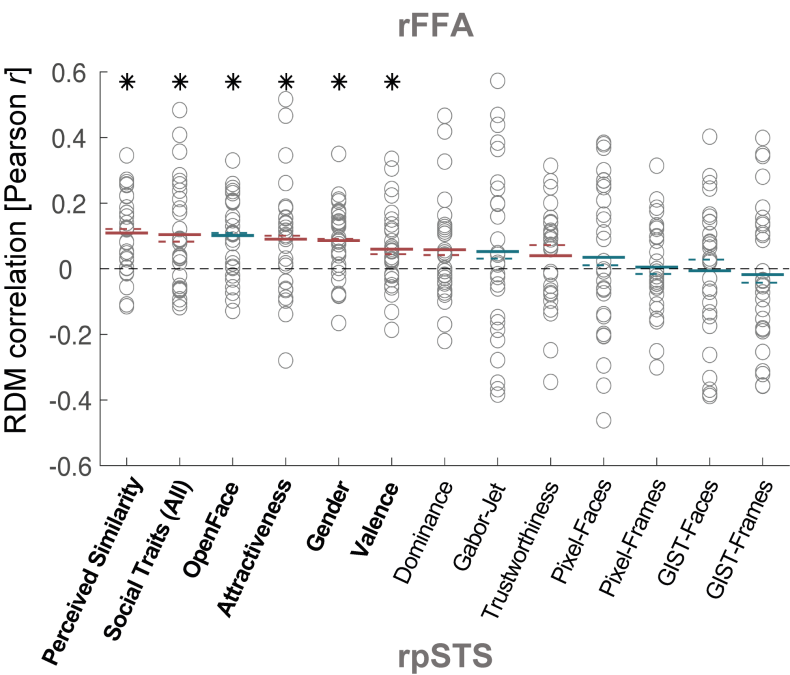
A**B****C****D**

A. Individual model analysis



B. Weighted model-combination analysis



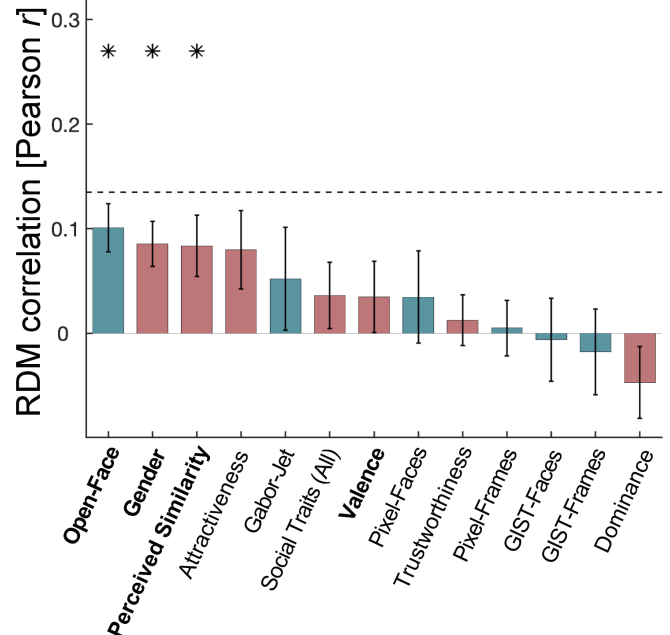
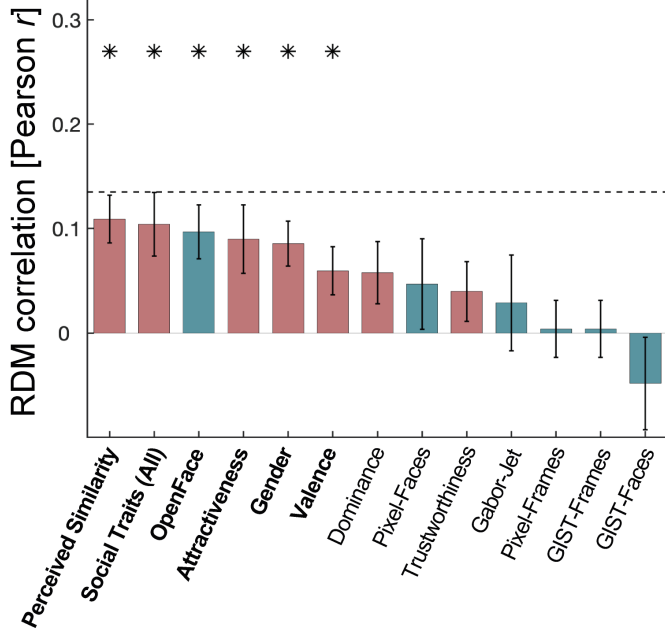


Perceived-property models (red line), Image-computable models (blue line)

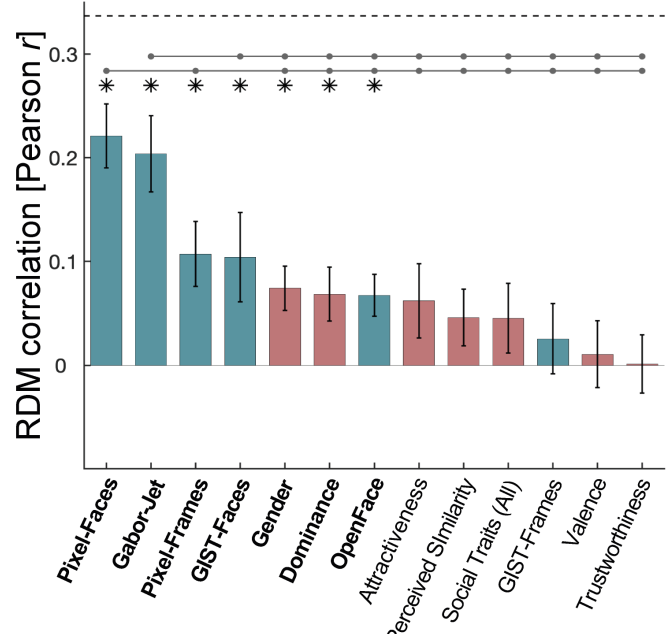
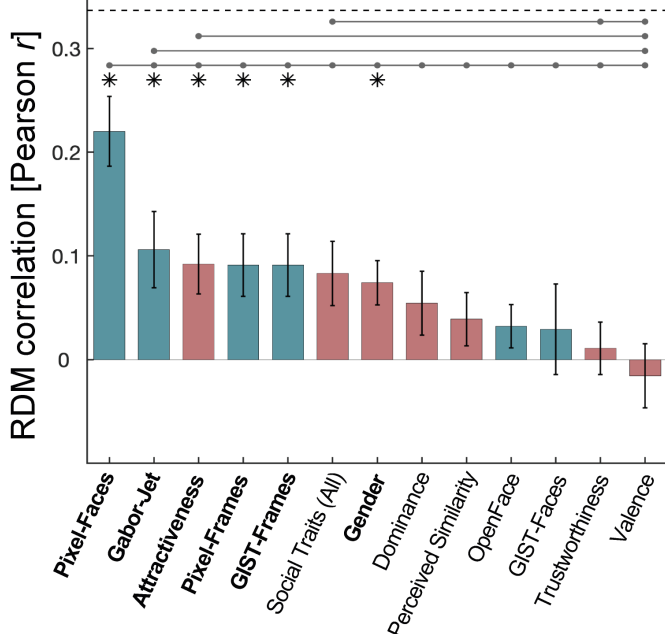
A. Image-computable models based on 72 images per video

B. Participant specific Perceived-property models

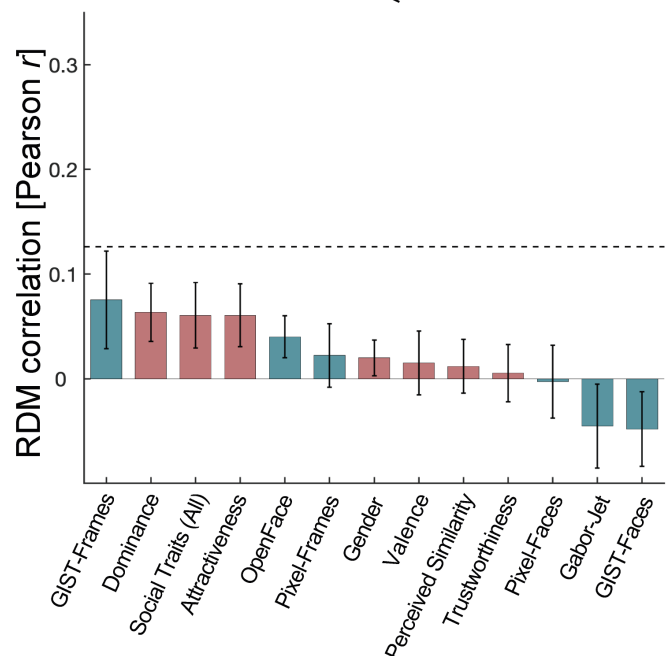
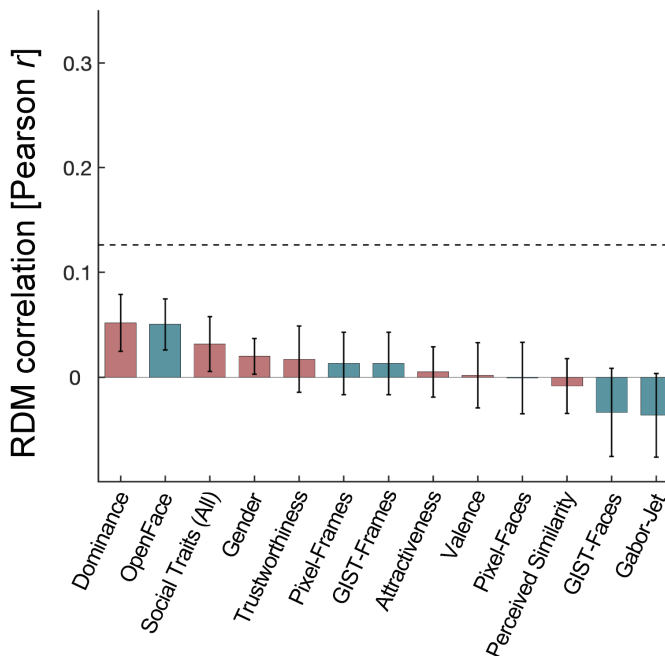
rFFA



rOFA



rpSTS



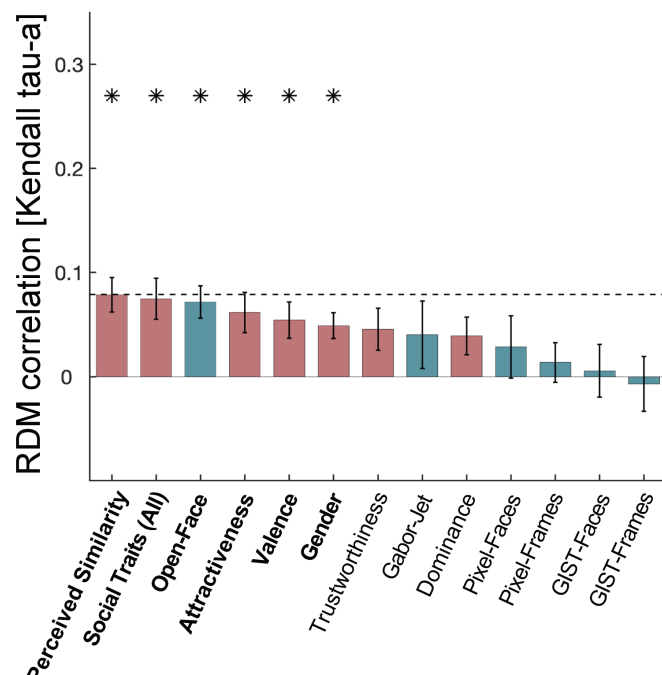
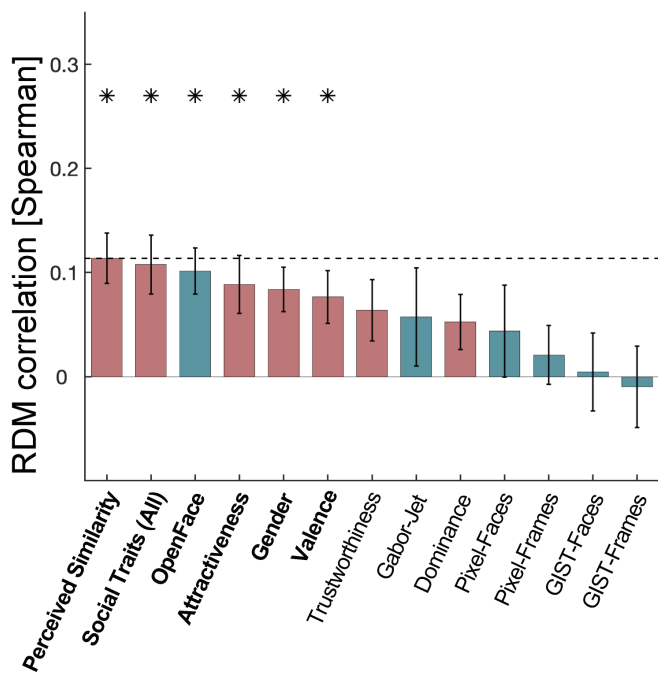
Perceived-property models

Image-computable models

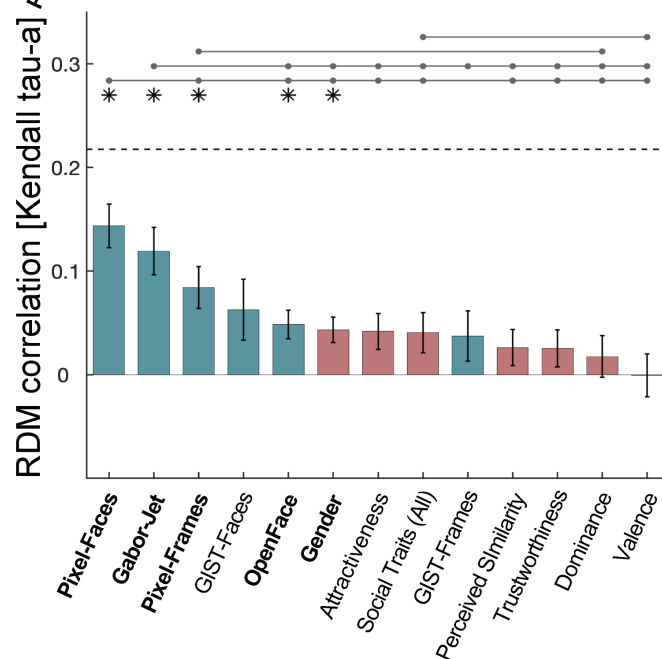
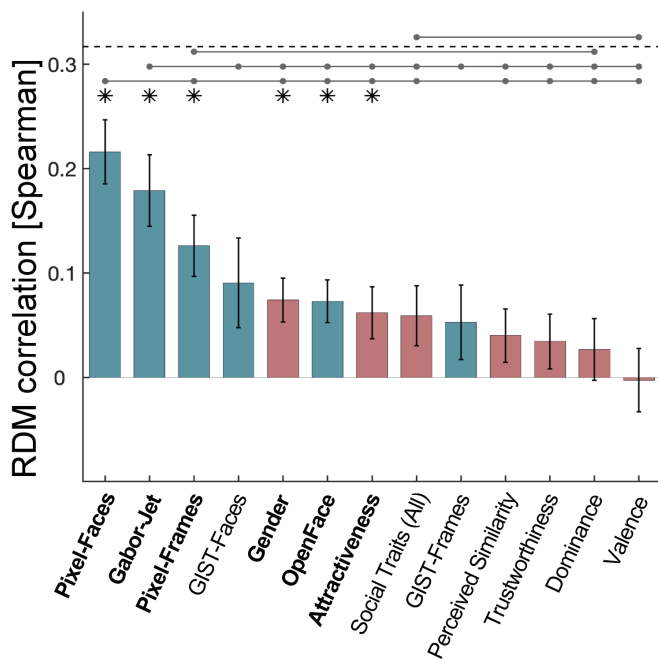
A. Spearman

B. Kendall tau-a

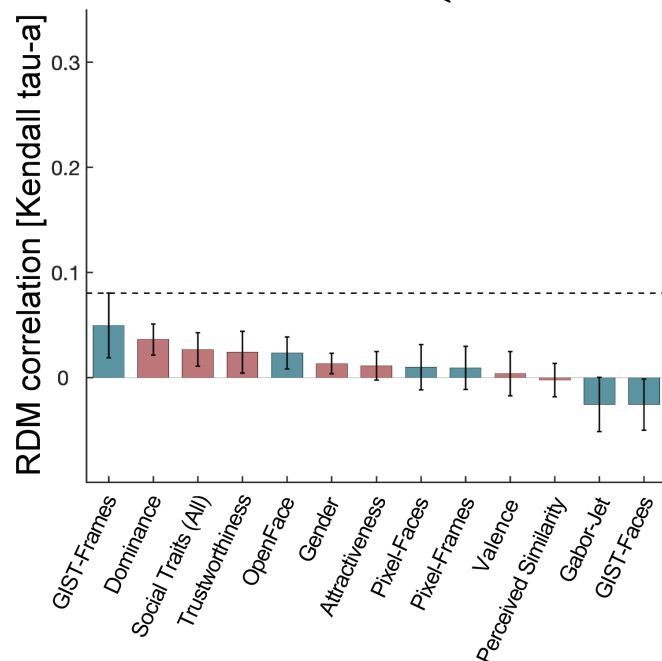
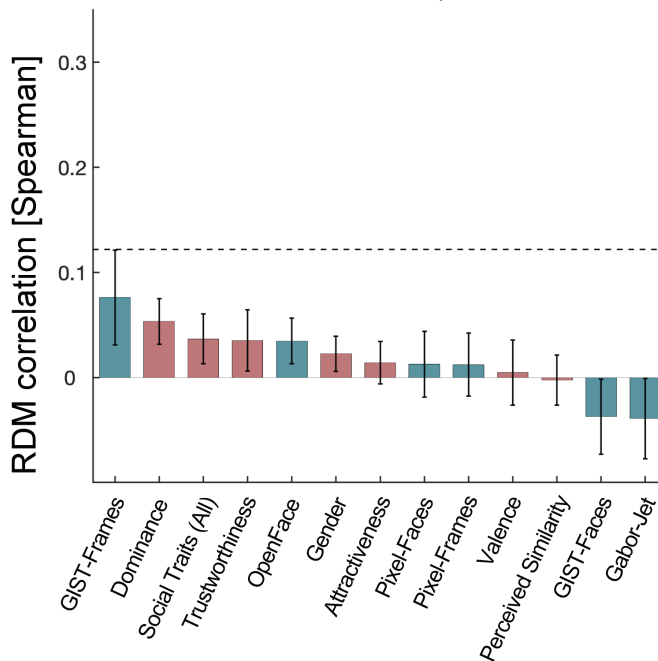
rFFA



rOFA



rpSTS

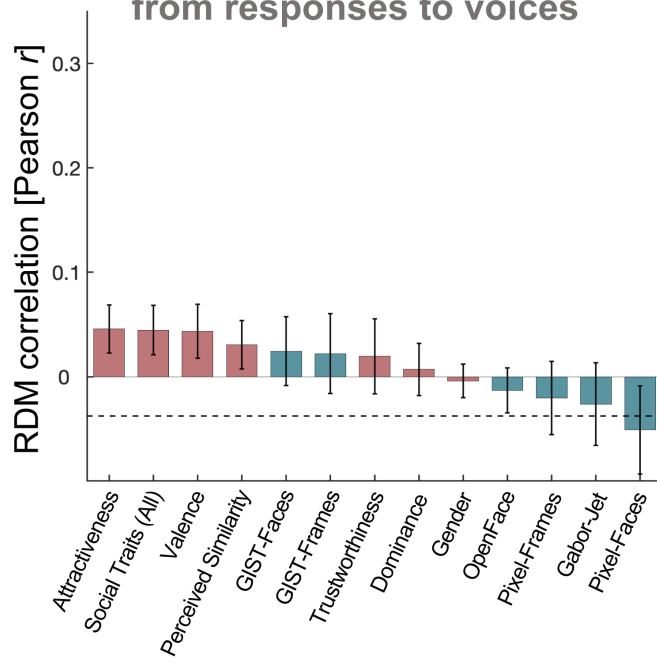


Perceived-property models

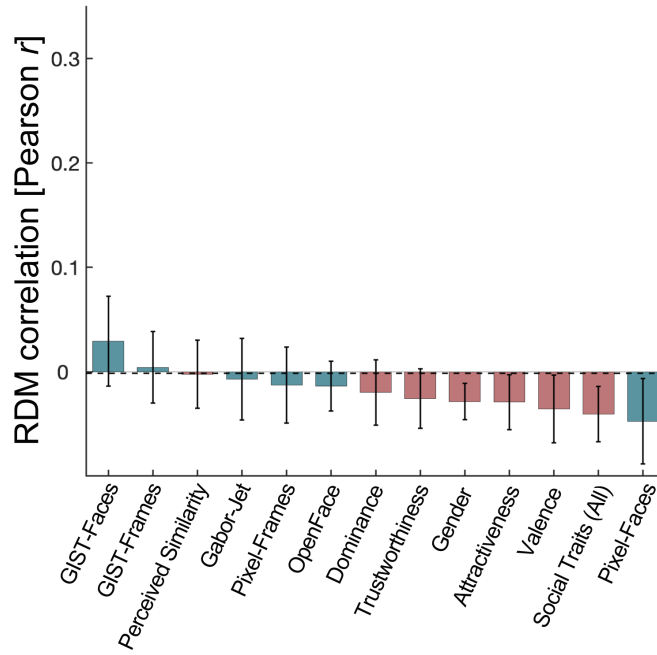
Image-computable models

Brain RDMs computed from responses to voices

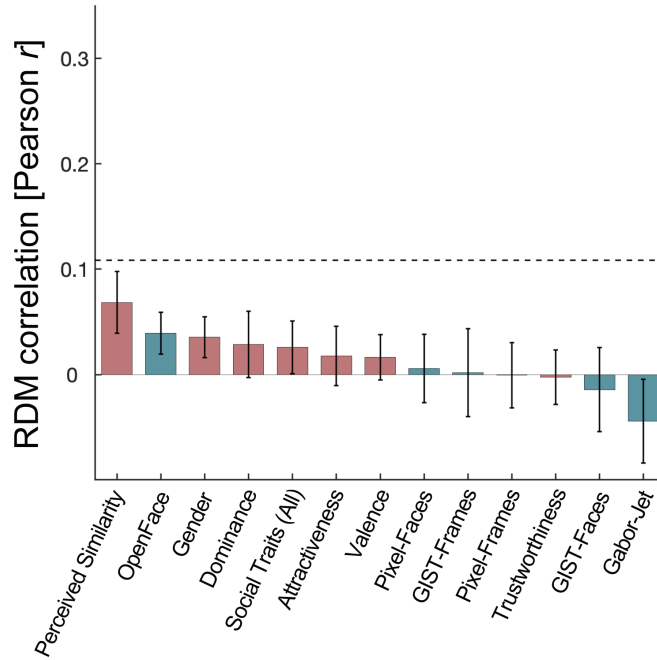
rFFA



rOFA



rpSTS



Perceived-property models Image-computable models

FFA and OFA encode distinct types of face identity information

— Extended data

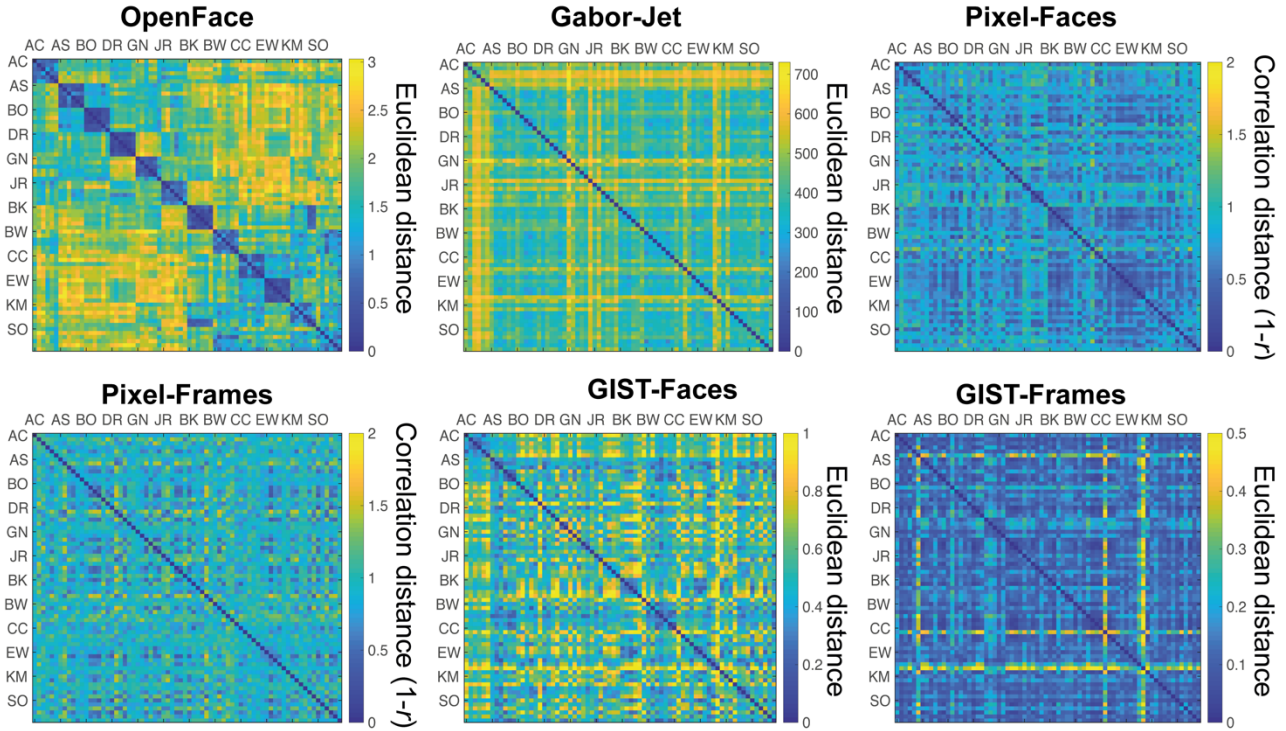
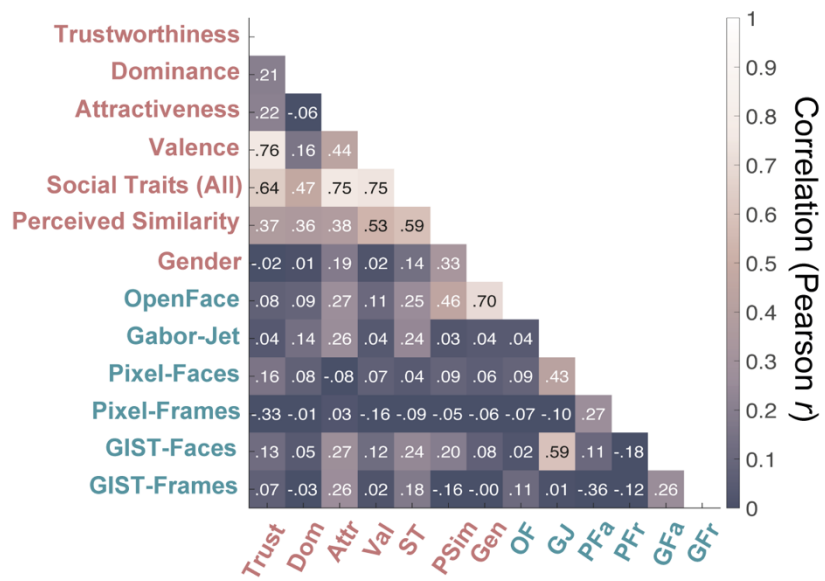


Figure 2-1. Image-computable model representational dissimilarity matrices (RDMs) per image. Model RDMs computed from dissimilarities between images for OpenFace, Gabor-Jet, Pixel-Faces, Pixel-Frames, GIST-Faces, and GIST-Frames. Each row/column represents a single image, and images are clustered by identity (6 images for each of the 12 identities). Each cell shows the dissimilarity between the two images in the corresponding rows and columns, with a value of zero indicating that images are identical. Matrices are symmetric around a diagonal of zeros. From these models, only the OpenFace model grouped different images of the same identity as more similar compared to images from different identities. [Please note that these full RDMs were not used in any analysis. Instead, we created 12x12 RDMs \(one entry for each of the 12 identities\) to be comparable to the brain RDMs \(Figure 2C\). To create the 12x12 RDMs, we computed the mean of all cells that showed images of the same identity pair.](#)

1
2



3

4 **Figure 2-2. Correlations (Pearson) between the different model RDMs.** The different candidate models
5 were compared with each other using Pearson correlation. This is the same figure as 2D, but with added
6 correlation values for each cell.

7